Damage ~~strength~~intensity increases ice mass loss from Thwaites Glacier, Antarctica

Yanjun Li[1, *], Violaine Coulon[2], Javier Blasco[2], Gang Qiao[3, *], Qinghua Yang[1], and Frank Pattyn[2]

[1]School of Atmospheric Sciences, Sun Yat-sen University, and Southern Marine Science and Engineering Guangdong Laboratory (Zhuhai), Zhuhai, 519082, China
[2]Laboratoire de Glaciologie, Université libre de Bruxelles, Brussels, 1050, Belgium
[3]College of Surveying and Geo-informatics, Tongji University, Shanghai, 200092, China

Correspondence to: Yanjun Li (liyj375@mail.sysu.edu.cn) and Gang Qiao (qiaogang@tongji.edu.cn)

Abstract. Ice damage, which results from the formation and development of crevasses on glaciers, plays a critical role in ~~determining~~ ice-shelf stability, grounding-line retreat, and subsequent sea-level rise~~, as it affects the formation and development of crevasses on glaciers. However~~. Yet, few ice-sheet models ~~have~~ explicitly ~~considered~~account for ice damage ~~nor~~or its ~~effect~~effects on glacier ~~projections~~dynamics. Here, we incorporate ice damage processes into an ice-sheet model~~. By applying the upgraded model~~ and apply it to the Thwaites Glacier basin~~, we further investigate~~ to assess the sensitivity of ~~Thwaites Glacier to the strength of the~~ mass loss to ice damage intensity. Our results indicate that, when accounting for ice damage mechanics, the ice-sheet model ~~enabled with the ice damage mechanics better~~ captures the observed ice geometry and mass balance of ~~the~~ Thwaites Glacier during the historical period (1990–2020~~), compared to the default model that ignores ice damage mechanics. Ice damage may result in a collapse of Thwaites Glacier on~~). On multidecadal-to-centennial timescales ~~and a notable increase in~~, ice damage facilitates the collapse of Thwaites Glacier, significantly increasing ice mass loss. ~~Moreover, ice mass loss from Thwaites Glacier~~When extending simulations to the ~~ocean may induce a sea-level rise of 5.0 ± 2.9 cm by~~year 2300, ~~which is~~ we show that accounting for ice damage results in more than ~~double~~twice the ~~simulation result without~~ ice ~~damage.~~ mass loss compared to simulations that neglect ice damage mechanics. This study highlights the ~~importance~~necessity of explicitly representing ice damage processes in ice-sheet models to improve projections of future ice loss and sea-level rise.

1 Introduction

~~Damage~~ The weakening of ~~glaciers~~ice due to the formation of large-scale crevasses and rifts, known as damage, is ~~getting more~~gaining attention due to its impact on glacier and ice sheet evolution ~~within~~in a warming climate. ~~Previous studies~~These fractures primarily form in fast-flowing regions such as near the grounding line or along shear margins, and are transported by ice flow, creating elongated fracture bands visible in satellite imagery (Albrecht and Levermann, 2012). Since the viscosity of these fracture bands is exceptionally low, they significantly influence the dynamics of the entire ice shelf (Khazendar et al., 2007; Borstad et al., 2012). Studies revealed that such damage ~~of glaciers~~ could ~~trigger~~initiate a feedback loop, promoting the further formation and propagation of rifts and crevasses~~, which increases the instability of~~ . This, destabilizes ice shelves by enhancing shearing ~~in the ice-shelf area~~, weakening ~~the ice-shelf structure, inducing~~their structural integrity, and ultimately leading to additional damage and ~~the~~ retreat of the grounding line (Sun et al., 2017; Lhermitte et al., 2020; Izeboud and Lhermitte, 2023). Moreover, the ability of ice shelves to restrain the ~~flow of~~ ice ~~from the upstream grounded glaciers towards the ocean (through the buttressing effect)~~flow weakens, leading to an acceleration of grounded ice mass loss and subsequent sea~~-~~-level rise. ~~Damage of~~Large-scale damage on glaciers ~~is~~could be a precursor of ice-shelf disintegration ~~and might~~, which may affect both the timing and magnitude of grounded ice loss, as well as the overall contribution of Antarctic glaciers to sea-level rise (Lhermitte et al., 2020; van de Wal et al., 2022; Izeboud and Lhermitte, 2023).

~~Damage~~ Several studies have investigated the influence of damage on the behavior of the Antarctic Ice Sheet (AIS). Borstad et al. (2012) applied a large-scale ice dynamical model to invert for damage on the Larsen B Ice Shelf prior to its collapse in 2002. They concluded that calving was triggered by the loss of load-bearing surface area due to fracturing. Albrecht and Levermann (2014) investigated the role of damage in softening ice across several Antarctic ice shelves using a fracture density field derived from observations. Gerli et al. (2023) demonstrated that the vertical propagation of crevasses within ice shelves can instantaneously increase the flux of upstream glaciers ~~has only been incorporated~~ . Huth et al. (2021, 2023) integrated a creep damage model into a ~~few ice~~ large-scale shallow-shelf ice flow model to simulate rift propagation leading to the formation of iceberg A68 from the Larsen C Ice Shelf. Damage is facilitated through hydrofracturing, and the combined effect of non-linear viscous rheology and damage processes within ice at water-filled crevasse tips can influence calving dynamics (Duddu et al., 2020). Sun and Gudmundsson (2023) conducted a series of numerical perturbation experiments to show that damage evolution significantly affects ice-shelf velocities and must be accounted for to accurately replicate observed velocity patterns. These studies reveal the interaction between damage processes and observed ice flow dynamics. They have one critical limitation, i.e., being diagnostic, which means that they investigate the instantaneous effect of damage on ice dynamics, but not the evolution of damage when ice thickness is allowed to evolve according to the applied changes. They therefore fail to predict future ice sheet ~~models to explore its potential impact on the ice~~ behavior or feedbacks induced by external changes, such as fracture enhancement due to atmospheric or oceanic forcing.

Prognostic modeling enables the assessment of ice sheet ~~dynamics under hypothetical ideal geometry conditions.~~and ice shelf evolution in response to fracture dynamics. However, most existing studies focus on idealized ice sheet geometries. Sun et al. (2017) coupled a continuum damage mechanics (CDM) model with an ice-sheet model based on the zero-stress Nye approach (Nye, 1957). ~~By applying the~~Applying this model to an ~~ideal ice sheet geometry (with retrograde bed slopes and strong lateral stress (Gudmundsson et al., 2012)) created by the Marine Ice Sheet Model Intercomparison Project~~ idealized ice-sheet geometry (MISMIP+; Cornford et al., 2020), they found that ice damage ~~results in a larger retreat of the~~ leads to greater grounding~~-~~-line retreat compared to ~~the simulation~~simulations without damage. Using the same model, Lhermitte et al. (2020) ~~demonstrated~~showed that intensifying damage at a specific location within ~~the~~ shear zones ~~leads to a broad~~triggers widespread propagation and amplification of damage ~~throughout the entire shear zone, reinforcing~~, supporting the hypothesis of ~~the~~a positive feedback mechanism. By integrating a continuum damage mechanics model with necking instability into an ice sheet model, Kachuck et al. (2022) simulated the evolution of the damage field and accurately predicted steady-state extents for a series of idealized, isothermal ice tongues and ice shelves. Similarly, Ranganathan et al. (2024) developed a damage evolution model coupled with a marine-terminating glacier flowline model and showed that damage can enhance mass loss from both grounded and floating ice. However, the results obtained from ~~tests of the ice-sheet model under ideal geometrical condition might not be~~ idealized geometries may not fully ~~applicable~~translate to the real world conditions, and ~~few~~ studies ~~have investigated~~investigating the ~~effect~~effects of ice damage on the ~~dynamic~~dynamics of ~~real-world ice sheets (e.g., Antarctic~~actual glaciers, such as Antarctic glaciers and ice shelves~~).~~, remain limited.

Extensive ice damage has been observed on Thwaites Glacier (TG), the largest ice stream in West Antarctica (2.1×10^5 km^2) and one of the fastest mass-losing outlet glaciers of the ~~Antarctic Ice Sheet (~~AIS~~)~~ (Rignot et al., 2019; Lhermitte et al., 2020; Surawy-Stepney et al., ~~2023a~~2023). Recent satellite images show an increase ~~of~~in ice-shelf damage ~~in TG (Bradley et al., 2023), with open rifts and dense crevasses distributing~~ across ~~its~~TG's floating ice shelf ~~(~~– both the Thwaites Eastern Ice Shelf (TEIS) and the Thwaites Western Glacier Tongue (TWGT~~)), as well as~~) – with open rifts and dense crevasses, also present in ~~the~~their shear zones ~~of both ice shelves~~ (Lhermitte et al., 2020). Episodic dynamic changes in TWGT, such as acceleration, have been ~~proven to be~~ linked to this damage. Miles et al. (2020) found ~~the~~that rapid acceleration ~~periods identified from~~phases observed between 2006~~ to ~~–2012 and 2016~~ to ~~–2018 ~~corresponded to~~ coincided with structural weakening. Similarly, Surawy-Stepney et al. (~~2023a) also~~2023) confirmed that the formation and ~~development~~evolution of crevasses along ~~the~~TWTG's shear margin ~~of the TWGT~~ from June 2017 to December 2018 and in early 2020 ~~consistent~~aligned with ~~the acceleration~~periods of increased ice flow~~ during these periods. Moreover, as~~. As a marine glacier (i.e., grounded below sea level; Fig. 1a) ~~over~~on a retrograde bed slope, TG is susceptible to marine ice-sheet instability (MISI) (Schoof, 2007; Pattyn, 2018). Ice damage may facilitate ~~the~~ grounding-line retreat ~~of TG~~ by ~~undermining the structural~~compromising ice-shelf integrity~~ of ice shelves~~ and reducing their buttressing effect on upstream glaciers. However, Gudmundsson et al. (2023) found that the ~~TEIS is not giving any~~floating ice shelves of TG provide limited buttressing~~ to the ice sheet, meaning, and that~~ the loss of ~~this~~these ice ~~shelf~~shelves would ~~not~~ have a ~~major~~minimal impact~~. Despite this, it remains imperative to consider the damage processes when modelling and projecting the evolution of TG under future climate change, as well as the contribution of~~ on overall ice~~ mass loss from the TG basin to global sea level rise~~-sheet stability.

In this study, the numerical ice-sheet model Kori-ULB (Pattyn, 2017; Coulon et al., 2024), ~~which~~modified to explicitly ~~represents the~~represent continuum damage mechanics (Sun et al., 2017), is ~~employed~~used to investigate the ~~effect~~impact of ice damage on the present~~-day~~ and near-future evolution of the TG basin. We aim to (i) evaluate and calibrate the ~~Kori-ULB~~ model using ~~the observational data on the contribution to sea-level rise and the net~~ satellite-based observations of present-day mass~~ balance in the TG basin; (ii) quantify the effect of damage on the grounding-line retreat, ice velocity and mass -~~change ~~of the TG basin with a historically calibrated ensemble; and (iii)~~ rates, and (ii) explore the sensitivity of ~~the~~ glacier retreat and mass loss in the TG basin to increased damage ~~strength~~intensity. We run an ensemble of simulations in which two key parameters controlling ice damage intensity are systematically perturbed and compare the results to two baseline experiments that neglect ice damage feedbacks.

2 Methods

2.1 Ice-sheet and damage model

The Kori-ULB ice-sheet model (Pattyn, 2017; Coulon et al., 2024) is a ~~2.5D~~vertically integrated, thermomechanical finite difference model that combines ~~Shallow Ice Approximation~~shallow-ice approximation with ~~Shallow Shelf Approximation~~shallow-shelf approximation (so-called hybrid model; Winkelmann et al., 2011). The Kori-ULB ice-sheet model has been ~~proven to be an effective tool~~used for large-scale ~~simulations~~simulation of the ~~Antarctic Ice Sheet~~AIS (Seroussi et al., 2020; Coulon et al., 2024~~). It can also be applied to~~), as well as small drainage basins with ~~divergent~~different ice geometries, such as ~~the hypothetical ice geometries proposed by the~~ MISMIP3d (Pattyn et al., 2013) and MISMIP+ (Cornford et al., 2020) experiments, and ~~the~~real-world drainage basins ~~in real world~~ (e.g., Thwaites Glacier basin; Kazmierczak et al., 2024). In Kori-ULB, the relationship between the deviatoric stress τ and the strain rate $\dot{\epsilon}$ is described by Glen's constitutive flow law:

$$2A\boldsymbol{\tau}^{n-1}\boldsymbol{\tau} = \dot{\boldsymbol{\epsilon}}\,, \qquad (1)$$

where A is Glen's flow law factor, dependent on the ice temperature, and n is the flow rate exponent, with n =3.

To investigate the ~~responses of ice dynamics, grounding-line retreat and mass change in~~dynamical response of the TG basin to ice damage and damage parametric perturbations, we couple the ice-sheet model ~~to~~with the continuum damage ~~model CDM. Damage (~~mechanics (CDM) model developed by Sun et al. (2017). This model establishes a direct link between the amount of damage and ice viscosity: the propagation of damage reduces the ice viscosity through Glen's flow law, leading to faster ice. This damage feedback is described by the integration of a damage factor $D(\tau)$ in Eq. (1):

$$2A\boldsymbol{\tau}^{2}\boldsymbol{\tau} = (1 - D(\boldsymbol{\tau}))^{3}\dot{\boldsymbol{\epsilon}}\,, \qquad (2)$$

with D (x, y, z) a scalar damage variable, taking values from 0 (undamaged ice) to 1 (ice entirely fractured by surface and basal crevasses). Given the integration over the vertical, this results in the following expression for the vertically integrated effective viscosity:

$$2h\mu = [h - d(\tau_1)]A^{-\frac{1}{3}}\dot{\boldsymbol{\epsilon}}^{-\frac{2}{3}}\,, \qquad (3)$$

where μ is effective viscosity, h is ice thickness, d~~(~~ $(x, y) \in [0, h\,(x, y)]$ is the vertical integral of D (x, y, z), and τ_1~~)) in~~ is the first principal stress. To determine the relationship between ice damage and the first principal stress $d(\tau_1)$, the CDM ~~includes~~framework is based on two key components: a local source of damage ~~$(d_1(\tau_1))$ and damage conservation~~term (d_1) that accounts for the local formation of damage, and an advection term (d_{tr}) that accounts for the transport of damage during ice flow ~~(d_{tr}). Damage conservation during ice flow (d_{tr}) describes the evolution of the vertically integrated damage field caused by advection, stretching, and mass loss or accumulation on the upper and lower surfaces of the glacier, which can be solved by a damage transport equation (Sun et al., 2017). The local source of damage $d_1(\tau_1)$ can be described by~~ .

In the absence of advection, ice damage is expressed as the total depth of the crevasses, i.e., the sum of surface crevasses d_s and basal crevasses d_b (Nick et al., 2011, 2013; Cook et al., 2014~~), which includes the depth of surface crevasses d_s and the~~

~~depth of basal crevasses d_b, and~~ ; Sun et al., 2017). Those can be calculated by the zero-stress ~~rule~~assumption (Nye, 1957; Nick et al., 2011):

$$d_s = \frac{\tau_1}{\rho_i g} + \frac{\rho_w}{\rho_i} d_w,$$ (~~1~~4)

$$d_b = \frac{\rho_i}{\rho_w - \rho_i}\left(\frac{\tau_1}{\rho_i g} - H_{ab}\right)$$ ~~,~~ (~~2,~~5)

~~$d_1(\tau_1) = max\,(0, ((d_s, d_s + d_b), C_1 * h)),$ (3)~~

where~~,~~ d_w is the water depth in the surface crevasse (here we only consider dry crevasses, so d_w is equal to 0), H_{ab} is the thickness above floatation, $g = 9.81$ m s^{-2} is the gravitational acceleration, and $\rho_i = 917$ kg m^{-3} and $\rho_w = 1028$ kg m^{-3} are the ice and seawater density, respectively. ~~τ_1 is the first principal stress, h is ice thickness and C_1 is a damage parameter that describes the upper limit of d_1 (τ_1) as a fraction of the ice thickness. The final relationship of damage ($d(\tau_1)$) is expressed as:~~

~~$d(\tau_1) = min(C_{tr} * h, max\,(d_1(\tau_1), d_{tr})),$ (4)~~

The local source of damage term $d_1(\tau_1)$ is then expressed as

$$d_1(\tau_1) = min(d_s + d_b, C_1 * h), \tag{6}$$

where~~, C_{tr}~~ C_1 is a ~~second damage~~ parameter ranging from 0 to 1 that ~~describes the~~ sets an upper limit ~~of d~~to $d_1(\tau_1)$ as a fraction of the ice thickness. This constraint prevents an overestimation of crevasse depth in the gridded domain.

In addition, damage fields are advected by ice flow. In this context, d_{tr} represents the evolution of the vertically integrated damage field caused by advection, stretching, and mass loss or accumulation at the glacier's upper and lower surfaces. The transported crevasses depth d_{tr} can be solved by the following damage transport equation (Sun et al., 2017):

$$\frac{\partial d_{tr}}{\partial t} + \nabla \cdot (\boldsymbol{u} d_{tr}) = -[max\,(\dot{a}, 0) + max\,(\dot{m}, 0)]\,\frac{d_{tr}}{h}, \tag{7}$$

The left-hand side of Eq. (~~C_1 is equal to or less than~~ 7) represents the conservation of vertically integrated damage, which includes the advection of crevasses with the ice flow and the effect of stretching and compression. On the right-hand side, damage reduction is modeled through two processes: an increase in undamaged ice thickness due to surface accumulation ($\dot{a}$) and erosion of the crevassed ice bottom by basal melting ($\dot{m}$).

Overall, at any given time and position (x, y, t), there exist two damage fields: the locally generated crevasse depth d_1 (x, y, t), as calculated above, and the advected crevasses depth d_{tr} (x, y, t). Assuming that crevasse surfaces do not bond together during closure, at least on the timescale relevant to crevasse closure (Sun et al., 2017), the final expression of damage d (x, y, t) is given by

$$d(x, y, t) = min(C_{tr} * h(x, y, t), max\,(d_1(x, y, t), d_{tr}(x, y, t))), \tag{8}$$

where C_{tr} is a parameter that limits d as a fraction of the ice thickness, with $C_1 \leq C_{tr}$. ~~A comprehensive description of the Kori-ULB ice-sheet model and its integration with the CDM model is given in Appendix A.~~This implies that regions of the ice shelf subjected to lower stress inherit damage from the upstream areas that are experiencing higher stress.

2.2 Simulation protocol

Simulations are spun up to a state representative of 1990, which then serve as the starting point for a 30-year historical run under constant present-day conditions. Surface mass balance (SMB) and air temperature are taken from the polar regional climate model MARv3.11 (Kittel et al., 2021), while ocean temperature and salinity are based on the data from Schmidtko et al. (2014). Basal melting underneath the floating ice shelves is estimated with the PICO model (Reese et al., 2018). Beyond the historical period (1990–2020), simulations are extended to 2300 under constant present-day atmospheric and oceanic conditions, allowing us to assess the effects of ice damage and the sensitivity of TG evolution over longer time scales. All simulations are performed at a spatial resolution of 2 km.

Two types of experiments are conducted (Table 1). First, we run an ensemble of simulations to investigate the impact of ice damage on the TG basin. To this end, we produce a perturbed parameter ensemble by systematically varying C_1 and C_{tr} (Eqs. 6 and 8), two key parameters governing damage feedback processes. We initially designed a 100-member ensemble, with C_1 and C_{tr} sampled within the range [0,1] using a Latin hypercube method. The ensemble was then reduced to 43 members to satisfy the requirement that $C_1 \leq C_{tr}$. The final 43-member ensemble is used to quantify the sensitivity of TG evolution to ice damage intensity.

Based on their performance during the historical simulations, ensemble members are categorized into two subgroups according to their ability to match satellite-based estimates of ice mass change in the TG basin (Shepherd et al., 2019). Simulations where the modeled ice mass change (i.e., the contribution to sea level, SLC) falls within the satellite-derived mean estimate ± two times the observed standard deviation (s.d.) are classified as Group 1 (G1). Those that significantly over- or underestimate this range (＞±2 s.d.) are classified as Group 2 (G2).

In addition, two control simulations without damage serve as baselines for comparison: one designed to reproduce observed mass-change rates (Ctrl$_{dhdt}$), and another without this constraint (Ctrl).

Table 1. Summary of the damage sensitivity experiments and two control experiments performed for the TG basin.

Experiments	**Description**	**Damage parameters**	
		C_1	C_{tr}
Ctrl	deactivated damage processes	–	–
Ctrl$_{dhdt}$	deactivated damage processes; corrected SMB using satellite-observed ice mass-change rates (Bevan et al., 2023)	–	–
Group 1	damage processes;	[0–0.23]	[0.2–1]

	SLC within the range of observational estimates ± 2 s.d. (0.24 ± 0.08 cm over 1992–2017) in the historical simulation (Shepherd et al., 2019)		
Group 2	damage processes; SLC outside the range of observational estimates ± 2 s.d. in the historical simulation	[0–0.53]	[0.1–1]

2.3. Model initialization ~~and simulation protocol~~

~~The Kori-ULB model uses the present-day ice sheet surface and bed geometry and grounding-line location from Bedmachine v2 (Morlighem et al., 2020) as input. Ice sheet~~ The initial conditions for both the 43-member damage ensemble and the Ctrl experiment are obtained ~~through the equilibrium initialization strategy~~ by an inverse simulation nudging towards present-day ice-sheet geometry (Pollard and DeConto, 2012; Bernales et al., 2017; Coulon et al., ~~2024). This results in an undamaged present-day~~2024), using present-day ice-sheet surface and bed geometry from BedMachine v2 (Morlighem et al., 2020) and present-day surface mass balance and air temperature from the polar regional climate model MARv3.11 (Kittel et al., 2021). A detailed description of the initialization procedure is provided in Appendix A of Coulon et al. (2024). The initial state for the Ctrl experiment is identical to that of the 43-member damage ensemble, ensuring that all start from the same ice sheet geometry. In the damage sensitivity experiments, ice damage is activated from the first timestep of the historical simulation, meaning that the ice sheet is considered undamaged at the start of 1990. Given that this assumption is somewhat idealized, the simulated damage can be interpreted as relative to the initial state.

To reproduce the dynamic disequilibrium observed during the historical period, we apply the initialization method of van den Akker et al. (2025). Specifically, the initial state of the Ctrl$_{dhdt}$ experiment is obtained by adding a 'correction term' – equal to minus the observed mass change rates (taken from Bevan et al., 2023) – to the present-day surface mass balance (Kittel et al., 2021) during the transient nudging procedure. This ensures that, by the time the nudging procedure has achieved a steady ~~state for 1990 (as shown in Fig. A1). After~~geometry, the model ~~initialization,~~has been trained to produce ice fluxes that closely match observations. In other words, the ice sheet model is 'trained' to equilibrate toward a state that implicitly accounts for observed mass change rates. As a result, it is important to note that the Ctrl$_{dhdt}$ experiment starts from a slightly different initial state than the Ctrl and damage experiments (see supplementary Figs. S1 and S2).

To evaluate the modeled initial conditions, we compute the root mean square errors (~~RMSEs~~RMSE) and the relative RMSE (rRMSE) between simulated and observed ice velocity (Rignot et al., 2017) and ice thickness (Morlighem et al., 2020):

$$RMSE = \sqrt{\frac{\sum_{i=1}^{n}(Sim_i - obs_i)^2}{n}} \tag{9}$$

$$rRMSE = \frac{RMSE}{\overline{obs}}, \tag{10}$$

where n is the number of grid points, sim_i and obs_i are the simulated and observed ice velocity (Rignot et al., 2017) or thickness (Morlighem et al., 2020), respectively, and $\overline{obs}$ is the mean observed ice velocity or thickness. In addition, we estimate the mean distance between the modeled and observed grounding-line position using the “open-ended box” approach of Moon and Joughin (2008).

Following the standard initialization procedure (used in the Ctrl and damage experiments), the RMSE (rRMSE) values between simulated and observed ice velocity and thickness are 201 m a^{-1} (~~786 m a^{-1} for the floating ice~~1.66) and 28 m (~~43 m for the~~ 0.01) for the whole basin, and 786 m a^{-1} (0.98) and 28 m (0.1) for floating ice~~), respectively. The~~ only (supplementary Fig. S1). The modeled grounding-line position of the TG basin ~~closely matches the observed grounding-line position~~ is in good agreement with observations (Gardner et al., 2018~~).~~

~~Starting from this~~), with an average offset of 1.3 km. For the initial state~~, we conduct an ensemble of simulations to explore the impact~~ of ~~ice damage on~~ the ~~dynamic evolution of~~Ctrl$_{dhdt}$ experiment, the ~~TG basin. We design a perturbed parameter ensemble including the two key parameters C_1 and C_{tr} (Eqs. 3 and 4) that govern the damage feedback processes. C_1 sets a limit on local damage and C_{tr} sets a limit on total damage. We initially create a 100-member ensemble by sampling C_1 and C_{tr} within the range of 0–1 using a Latin hypercube sampling method. The members in our ensemble are subsequently reduced to 43 to meet the requirement that $C_1 < C_{tr}$. Finally, the ensemble with 43 parameter members is used to quantify the sensitivity of TG evolution to the strength of ice damage.~~

~~We conduct an ensemble of historical simulations for 30 years (1990–2020) under present-day conditions with each of the 43 parameter members (Table A1). Based on the results from these historical simulations, the parameter~~RMSE (rRMSE) values of ~~C_1 and C_{tr} are further constrained by the satellite-based estimate of ice mass change in the TG basin (Shepherd et al., 2019). Parameter members that enable the simulated ice mass change (the contribution to sea-level rise and net mass balance) in the TG basin being within the range between the mean value of satellite-based estimate ± two times of the observed standard deviation (s.d.) are considered appropriate. These parameter members are then classified as Group 1 (G1). If the tested parameter member drastically over- or underestimates (beyond +/- 2 s.d.)) the observed ice mass change in the TG basin, it is classified as Group 2 (G2).~~

~~Two control simulations (Table 1 and Table A1) without damage are used as a baseline for comparison. One is designed to reproduce the observed mass change rates (the Ctrl$_{cal}$ experiment), while the other is not (the Ctrl experiment). In the Ctrl$_{cal}$ experiment, we force the model to reproduce the historical trends by integrating satellite-based data of present-day ice mass change rates in the TG basin (Otosaka et al., 2023), thereby facilitating ice thinning at the beginning of the run. The Ctrl$_{cal}$ experiment matches observed trends relying on different physics compared to the damage experiments. Consequently, the differences in the dynamic changes of TG between experiments with or without considering damage can be used to quantify the impact of damage strength on its future dynamics.~~

~~We employ the method described in van den Akker et al. (2024) to derive the initial state of the Ctrl$_{cal}$ experiment (Fig. A2). After model initialization, RMSEs of~~ ice velocity and thickness ~~for this initial state~~ are 172 m a^{-1} (1.42) and 27 m (0.01) for the whole basin, and 659 m a^{-1} (0.83) and 54 m (0.13) for ~~the~~ floating ice~~) and 27 m (54 m for the floating ice), respectively. The initial~~ only (supplementary Fig. S2). The modeled grounding-line position also closely ~~matches the observed grounding-line position. At the start of the historical run, the present-day SMB is reinstated without the additional mass-change term.~~

~~Hence, by construction, the simulated ice sheet reproduces the observed mass-change rates. Note that the initial state for the Ctrl experiment is the same as that used in the damage sensitivity experiments. After the historical period, simulations are extended until the year 2300, with constant atmospheric and oceanic forcing at present-day conditions, to assess the effect of damage and the potential response and sensitivity of TG evolution to the strength of ice damage at larger time scales.~~

aligns with observations, with an average offset of 2.3 ~~Forcing data~~km.

~~Initial present-day surface mass balance and temperature are obtained from the polar regional climate model MARv3.11 (Kittel et al., 2021). Present-day ocean temperature and salinity are derived from data provided by Schmidtko et al. (2014). Please see Table A2 for all forcing and model calibration and evaluation data used in this study. The basal melting underneath the floating ice shelves is estimated using the PICO model by Reese et al. (2018). All simulations in this study are performed at a spatial resolution of 2 km.~~

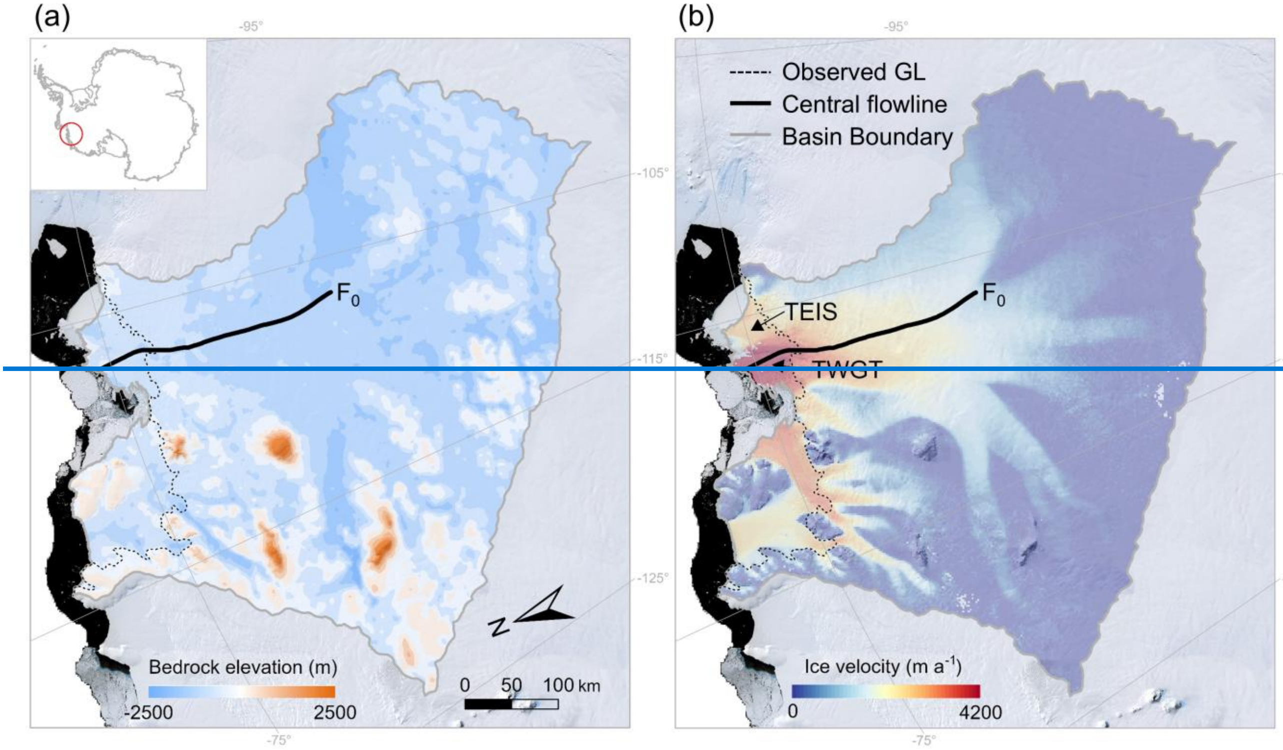

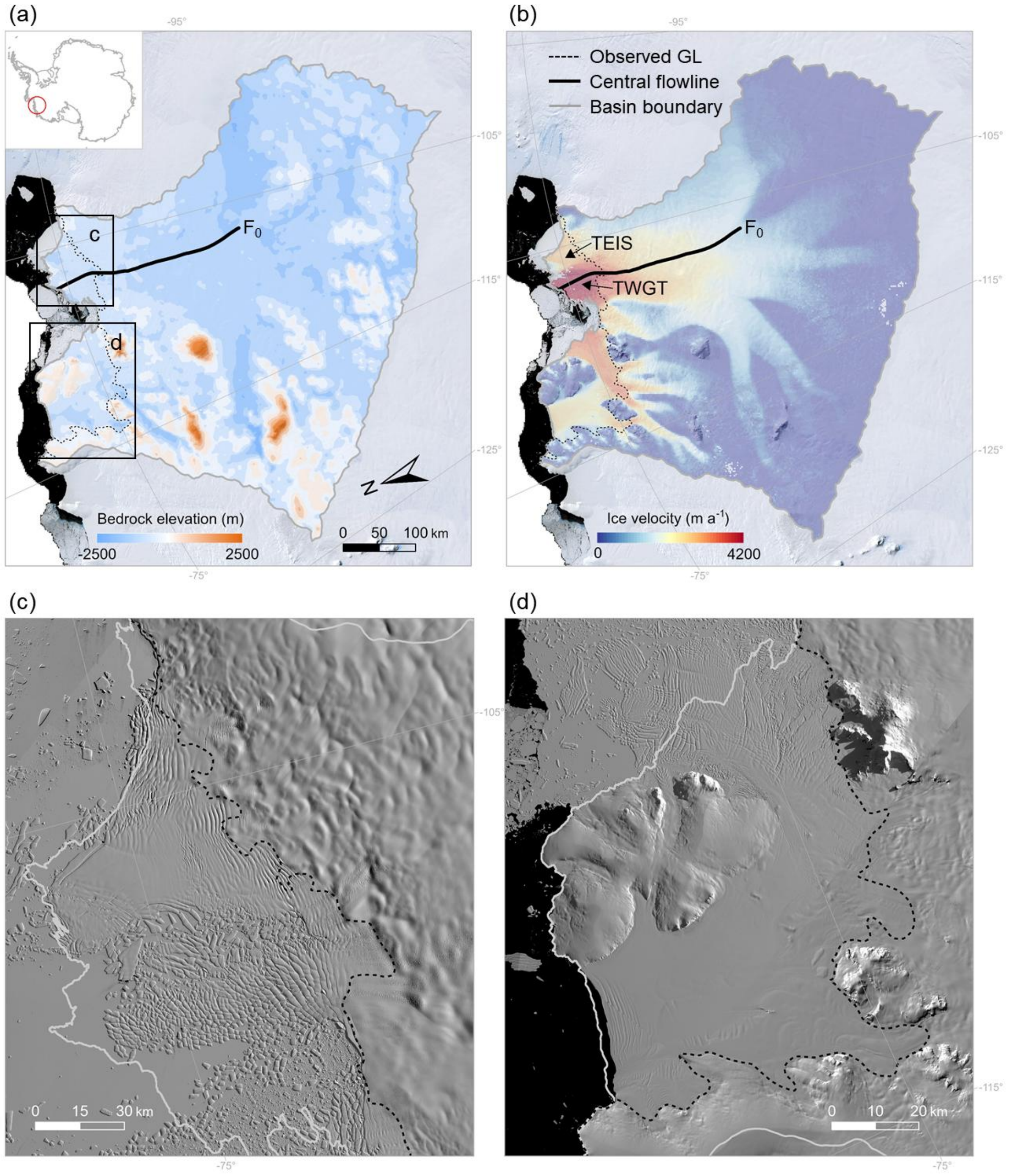

Figure 1. Bedrock elevation and ice velocity in the TG basin. (a) Observed bedrock elevation of the TG basin based on BedMachine v2 data (Morlighem et al., 2020) and (b) observed ice velocity of the TG basin based on Making Earth System Data Records for Use in Research Environments (MEaSUREs~~ data~~) InSAR-Based Antarctica Ice Velocity Map, Version 2 (Rignot et al., 2017) ~~overlapped~~overlaid on the Landsat ~~image mosaic~~Image Mosaic of Antarctica (LIMA~~) mosaic (~~; Bindschadler et al., 2008). The solid black~~ solid~~ curve is the central flowline profile stemming from the Antarctic surface flowline dataset developed by Liu et al. (2015), which spans 340 km from the inland grounded ice (F_0) to the calving front. The ~~black ~~dashed black line shows the position of the observed grounding line (Gardner et al., 2018). The inset in panel (a) shows the location of the TG basin in Antarctica. TEIS represents the Thwaites Eastern Ice Shelf and TWGT represents the Thwaites Western Glacier Tongue. The black rectangular insets in panel (a) are panels (c) and (d), which show the crevasse distributions

across the ice shelf regions in the TG basin, based on Landsat-8 satellite images acquired in December 2020. The gray line is the basin boundary of the TG basin derived from Zwally et al. (2015).

3 Results

3.1 Effects of ice damage on the simulated historical evolution of Thwaites Glacier (1990–2020)

The ~~45~~43-member ensemble of simulations over 1990–2020 in the TG basin ~~show~~shows a ~~high~~strong sensitivity ~~of mass loss~~ to ~~the strength of~~ ice damage (Fig. 2~~).~~), resulting in a wide spread of mass change estimates. The simulated ~~contribution of~~ ice mass ~~change~~loss ranges from ~~-291.54~~0.03 to ~~-9.37 Gt a~~$^{-}$1.~~ Of all~~ 42 cm sea-level equivalent (SLE). Among the 43 parameter ~~members of~~sets for C_1 and C_{tr}, ~~15 members~~16 are classified into Group 1 (Table 1~~ and~~, supplementary Table ~~A1,~~S1, and light green lines in Fig. 2~~). The~~), while the remaining ~~28 members are classified~~27 fall into Group 2 (light red lines in Fig. 2). In Group 1, the simulated ~~net~~ ice mass change in the TG basin ranges from ~~-54.28~~0.16 to -0.31~~.75 Gt a^{-1}~~ cm SLE, with ~~the highest mass loss estimate being 1.7~~a mean change of 0.24 ± 0.04 cm SLE. In comparison, the mean of Group 2 is 0.62 ± 0.36 cm SLE, that is 2.5 times ~~of the lowest estimate~~larger.

~~**Table 1.** Summary of the typical damage sensitivity experiments and two control experiments performed at the TG basin.~~

~~**Experiments**~~	~~**Description**~~	~~**Damage parameters**~~	
		~~C_1~~	~~C_{tr}~~
~~Ctrl~~	~~deactivated damage processes~~	–	–
~~Ctrl$_{cal}$~~	~~deactivated damage processes &~~ ~~satellite-observed mass balance calibrated (Otosaka et al., 2023)~~	–	–
~~Group 1~~	~~damage processes &~~ ~~SLC and net mass balance within the range of observational estimates ± 2 s.d. (0.24 ± 0.08 cm and -46.1 ± 14.4 Gt a^{-1} over 1992–2017) in the historical simulation (Shepherd et al., 2019)~~	~~[0–0.24]~~	~~[0.2–0.8]~~
~~Group 2~~	~~damage processes &~~ ~~SLC and net mass balance outside the range of observational estimates ± 2 s.d. in the historical simulation~~	~~[0–0.56]~~	~~[0–1]~~

The explicit representation of ice damage processes better captures the observed ice mass change in the TG basin compared to the default model without damage (Ctrl experiment in Fig. 2). ~~The~~ For the period 1990–2020, the simulated mean ~~value of~~net mass ~~change~~balance for Group 1 (with damage) is -~~38.3~~26.5 Gt a^{-1}, which is comparable to satellite-derived observations (-46.1 ± ~~14.4~~7.2 Gt a^{-1} over 1992–2017; mean ± ~~2~~1 s.d.). ~~Ignoring~~In contrast, neglecting ice damage underestimates ice mass change ~~(-2.1 Gt a^{-1};~~ by more than an order of magnitude, with the Ctrl experiment ~~in Fig. 2). In contrast, the Ctrl$_{cal}$~~simulating only 1.2 Gt a^{-1}. The Ctrl$_{dhdt}$ experiment, which ~~uses~~also ignores ice damage but applies an artificial ~~calibration of~~correction to the ice mass~~-~~-change rate, ~~reproduces~~yields a simulated net mass ~~change (-28~~balance of -30.1 Gt a^{-1}~~)~~ over 1990–2020, comparable to ~~the~~ estimates ~~for~~from Group 1.

~~Ice damage processes also result in a larger grounding-line retreat (Fig. 2c and Fig. A3).~~ By 2020, the simulated grounding lines ~~by the ensemble of~~from Group 1 (~~the~~dashed green lines in Fig. 2c) ~~retreat by~~have retreated 6~~–10~~–14 km ~~further~~inland along the central ~~profile than the observed grounding-line~~flowline compared to their initial position (~~Gardner et al., 2018; the black~~ dashed light gray line in Fig. 2c). ~~All simulated grounding lines in Group 2 also show~~This corresponds to a ~~larger~~ retreat ~~by~~ rate of 0.2–0.5 km a^{-1} over 1990–2020 ~~than the observed grounding-line position (Fig. 2c), with the maximum retreat being about 44 km~~ along the central flowline profile ~~and a retreat rate of up to 1.5 km a^{-1} (the red line~~(green lines in Fig. ~~A3). This retreat rate is twice the observed~~ 3), similar in magnitude to observations, which indicate a mean annual retreat rate ~~(∼~~of 0.7 km a^{-1}~~)~~ over 1992–2011 (Rignot et al., 2014) and ~~2 to 5 times of the observed annual retreat rate (~~of 0.3–0.6 km a^{-1}~~)~~ over 2011–2017 (Milillo et al., 2019). ~~In addition, the grounding-line positions simulated by the two~~In contrast, the simulated grounding lines of Group 2 retreat at rates of up to 1.5 km a^{-1} along the central flowline profile, resulting in a total retreat of up to 44 km upstream the initial grounding-line position by 2020 (Fig. 2c and red line in Fig. 3). While both control experiments ~~that ignore damage~~ show ~~an overall~~reduced retreat along the central flowline profile during the historical simulation period (Fig. ~~A3). The simulated~~ 2c), the grounding-line ~~position in the Ctrl$_{cal}$ experiment shows a~~ retreat ~~comparable to those simulated in the Group 1 experiments in the~~ in the eastern section of TG~~.~~ in the Ctrl$_{dhdt}$ experiment is comparable to that of Group 1 (Fig. 3). In contrast, the retreat ~~simulated~~ in the Ctrl experiment ~~is~~remains relatively minor. ~~Along the central profile of TG, the simulated grounding-line positions of the two control experiments are even more seaward than the satellite-based observation (Fig. 2c and Fig. A3).~~

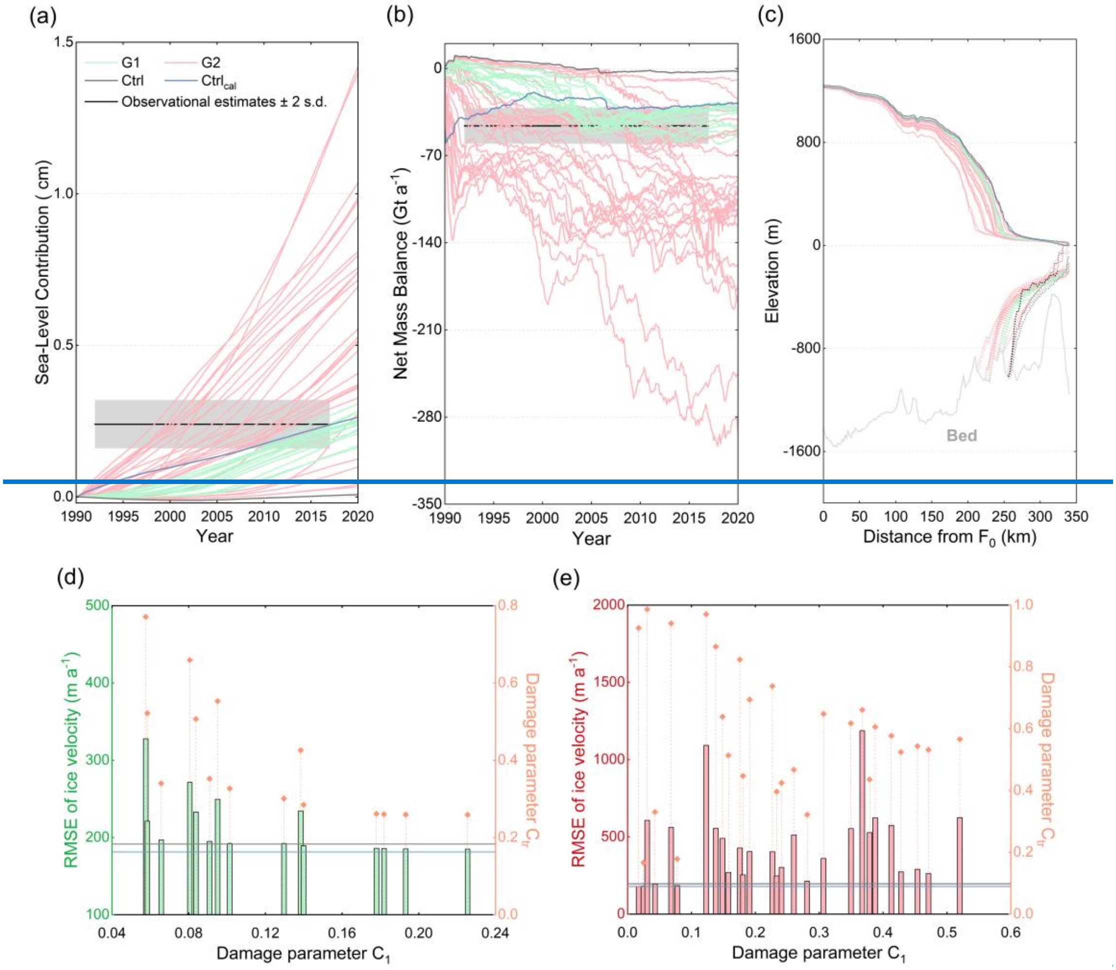
(a)
G1
G2
Ctrl
Ctrl$_{cal}$
Observational estimates ± 2 s.d.
Sea-Level Contribution (cm)
1.5
1.0
0.5
0.0
1990
1995
2000
2005
2010
2015
2020
Year
(b)
Net Mass Balance (Gt a^{-1})
0
-70
-140
-210
-280
-350
1990
1995
2000
2005
2010
2015
2020
Year
(c)
Elevation (m)
1600
800
0
-800
-1600
Bed
0
50
100
150
200
250
300
350
Distance from F$_0$ (km)
(d)
RMSE of ice velocity (m a^{-1})
500
400
300
200
100
Damage parameter C$_{tr}$
0.8
0.6
0.4
0.2
0.0
0.04
0.08
0.12
0.16
0.20
0.24
Damage parameter C$_1$
(e)
RMSE of ice velocity (m a^{-1})
2000
1500
1000
500
0
Damage parameter C$_{tr}$
1.0
0.8
0.6
0.4
0.2
0.0
0.0
0.1
0.2
0.3
0.4
0.5
0.6
Damage parameter C$_1$

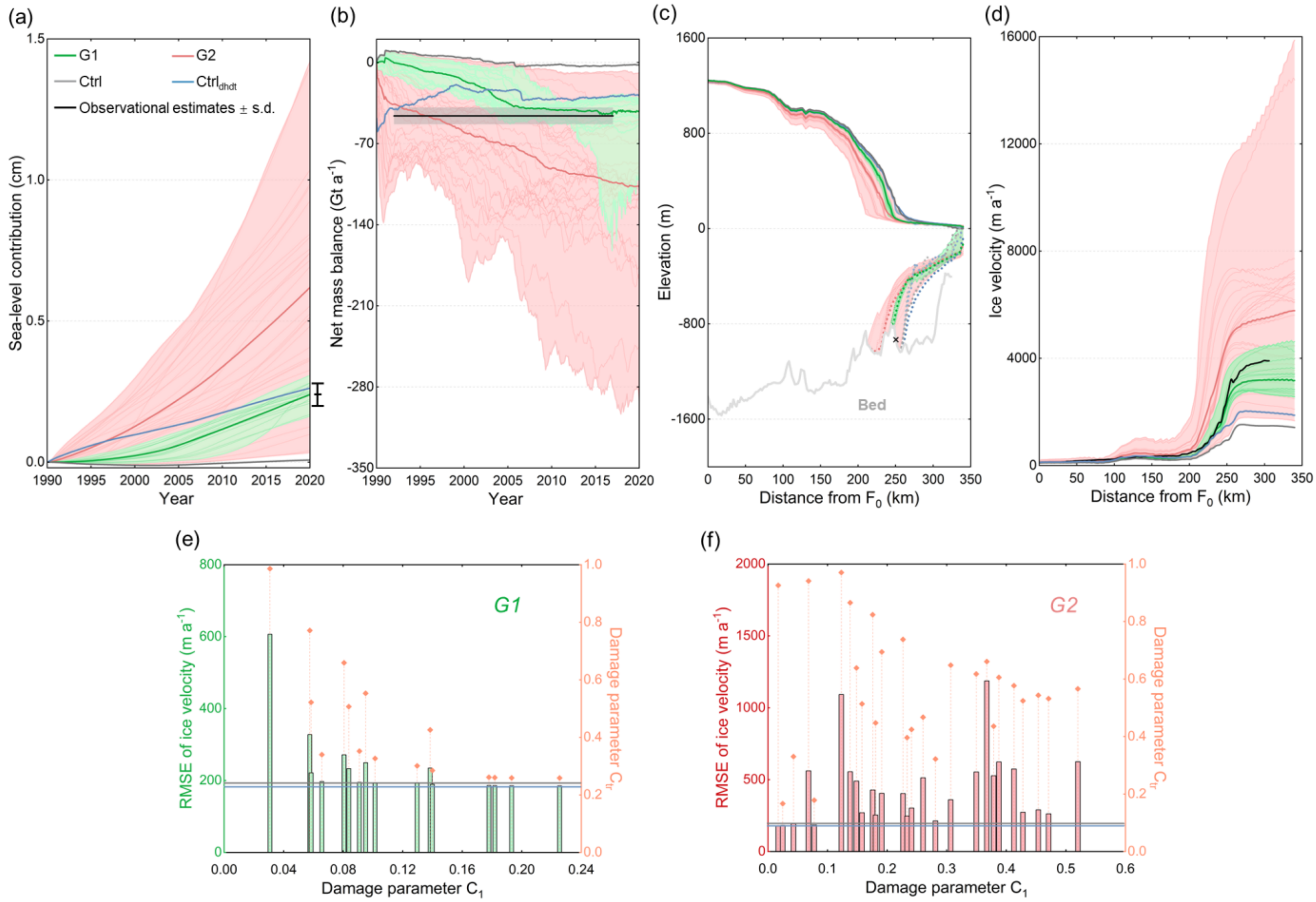

Figure 2. ~~The simulated~~Simulated change trends of ice mass balance and grounding-line position in the TG basin under different damage ~~strengths~~intensities over the period 1990–2020. (a) ~~Contribution~~the simulated contribution of ice mass loss in the TG basin to ~~global~~ sea-level~~ rise~~; (b) the net mass balance (~~considers~~considering volume above flotation only, i.e., the rate of mass change contributing to sea-level rise) in the TG basin; (c) the geometry profiles along the central flowline profile (~~the~~solid black ~~curve~~line in Fig.1) and the simulated (dashed red and green ~~dashed~~ lines) ~~and observed (black dashed line)~~ grounding-line positions; (d) the simulated ice velocity along the central flowline profile. RMSEs between the simulated and observed ice velocity under different parameter combinations of C_1 and C_{tr} in (~~d) Group 1 and (~~e) Group 1 and (f) Group 2. The dark red and green lines in panels (a)–(d) represent the mean, and the hatched area represents the ensemble range, i.e., spread between maximum/minimum values. The black lines and shaded areas in panels (a) and (b) represent the observed mean value ± ~~2~~1 standard deviation (Shepherd et al., 2019). The ~~grey~~gray line represents the simulation result ~~by~~of the model that ignored ice damage processes and did not integrate satellite-based ~~observation~~observations of present-day mass~~-~~change rates to constrain the model initialization (Ctrl experiment), and the blue line represents the simulation result ~~by~~of the model that ignored ice damage processes but integrated satellite-based ~~observation~~observations to constrain the model initialization (~~Ctrl_{cal}~~Ctrl_{dhdt} experiment). In panel (c), the dashed light gray and blue lines represent the initial grounding-line positions for the Ctrl/damage experiments and the Ctrl_{dhdt} experiment, and the black cross marks the location of the observed grounding-line position (Gardner et al., 2018).

~~The RMSEs between the observed and simulated ice velocities in the Ctrl$_{cal}$ and Ctrl experiments are 181 m a^{-1} (753 m a^{-1} for the floating ice) and 191 m a^{-1} (745 m a^{-1} for the floating ice), respectively (Fig. 3). Incorporation~~

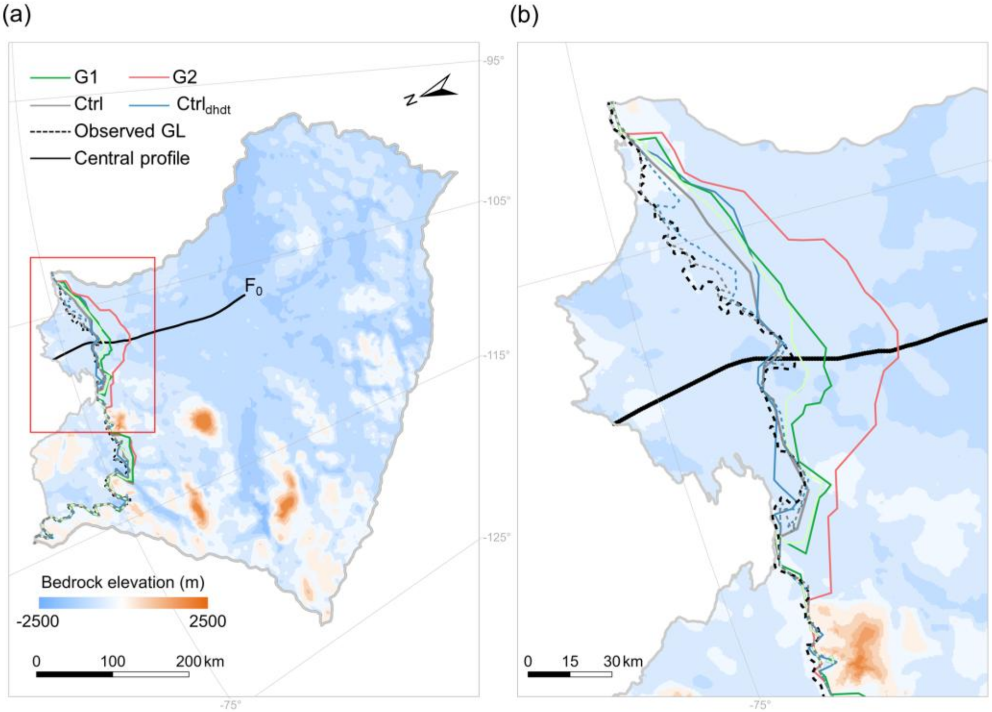

Figure 3. Spatial pattern of the grounding-line positions in the TG basin over the historical period 1990–2020 under different damage intensities. (a) Evolution of the grounding-line positions within the TG basin and (b) an enlarged view of the red box in (a). The light green and dark green lines represent the experiments with the least and the most grounding-line retreat in Group 1, and also correspond to the experiments with the lowest and highest damage intensity in Group 1. The red line represents the experiment with the most grounding-line retreat in Group 2 and also corresponds to the experiment with the highest damage intensity in Group 2 over the historical period 1990–2020. The dashed black line presents the observed grounding-line position (Gardner et al., 2018). The solid blue and gray lines present simulated grounding-line positions of the Ctrl$_{dhdt}$ and Ctrl experiments in 2020, respectively. The background image in panel (a) is the observed bedrock elevation of the TG basin derived from BedMachine v2 data (Morlighem et al., 2020), while the solid black curve indicates the central flowline profile stemming from the Antarctic surface flowline dataset developed by Liu et al. (2015), spanning 340 km from the inland grounded ice (F$_0$) to the calving front. The solid light gray line delineates the TG basin boundary based on Zwally et al. (2015). The dashed gray and blue lines are the initial grounding-line positions of the Ctrl/damage experiments and the Ctrl$_{dhdt}$ experiment, respectively.

The incorporation of ice damage induces a notable ~~change~~increase in ~~the~~ simulated ice ~~flow~~ velocity over the historical period (Figs. 2d~~–2e~~2f and Fig. ~~3~~4). By 2020, the mean RMSEs (rRMSEs) of simulated ice velocities in Group 1 and Group 2 simulations are ~~216 ± 40~~241 ± 102 m a^{-1} (1.6) and 435 ± 247 m a^{-1} (~~897 ± 177 m a^{-}~~1.9) for the ~~floating ice)~~whole basin, and ~~441 ± 245~~995 ± 417 m a^{-1} (~~1693 ± 877 m a^{-}~~1.2) and 1665 ± 880 m a^{-1} (1.5) for floating ice only. For comparison, the RMSEs (rRMSEs) between observed and simulated ice velocities in the Ctrl$_{dhdt}$ and Ctrl experiments are 181 m a^{-1} (1.5) and 191 m a^{-1} (1.58) for the whole basin, and 753 m a^{-1} (0.97) and 745 m a^{-1} (0.92) for ~~the~~ floating ice~~), respectively~~ only. This suggests that the parameter ~~members, which enable to reasonably capture~~values enabling a reasonable reproduction of the observed ice mass ~~balance~~loss in the TG basin (i.e~~.~~., the ensemble of Group 1~~), also ensure that the model can better reproduce the observed)~~

also allow for a reasonable representation of ice velocity~~. For ~~, whereas those in Group 2 lead to significantly larger discrepancies (Fig. 2d). Among all Group 1 simulations~~ with activated damage processes in~~, the ~~model, the~~lowest RMSE between observed and simulated ice velocity ~~is the lowest ~~occurs when ~~C_1~~C_I and C_{tr} are set to 0.23 and 0.26, respectively~~.~~ (Figs. 4a–d). Along the central flowline, ignoring damage largely underestimates the ice flow speeds that are currently observed (Fig. 2d).

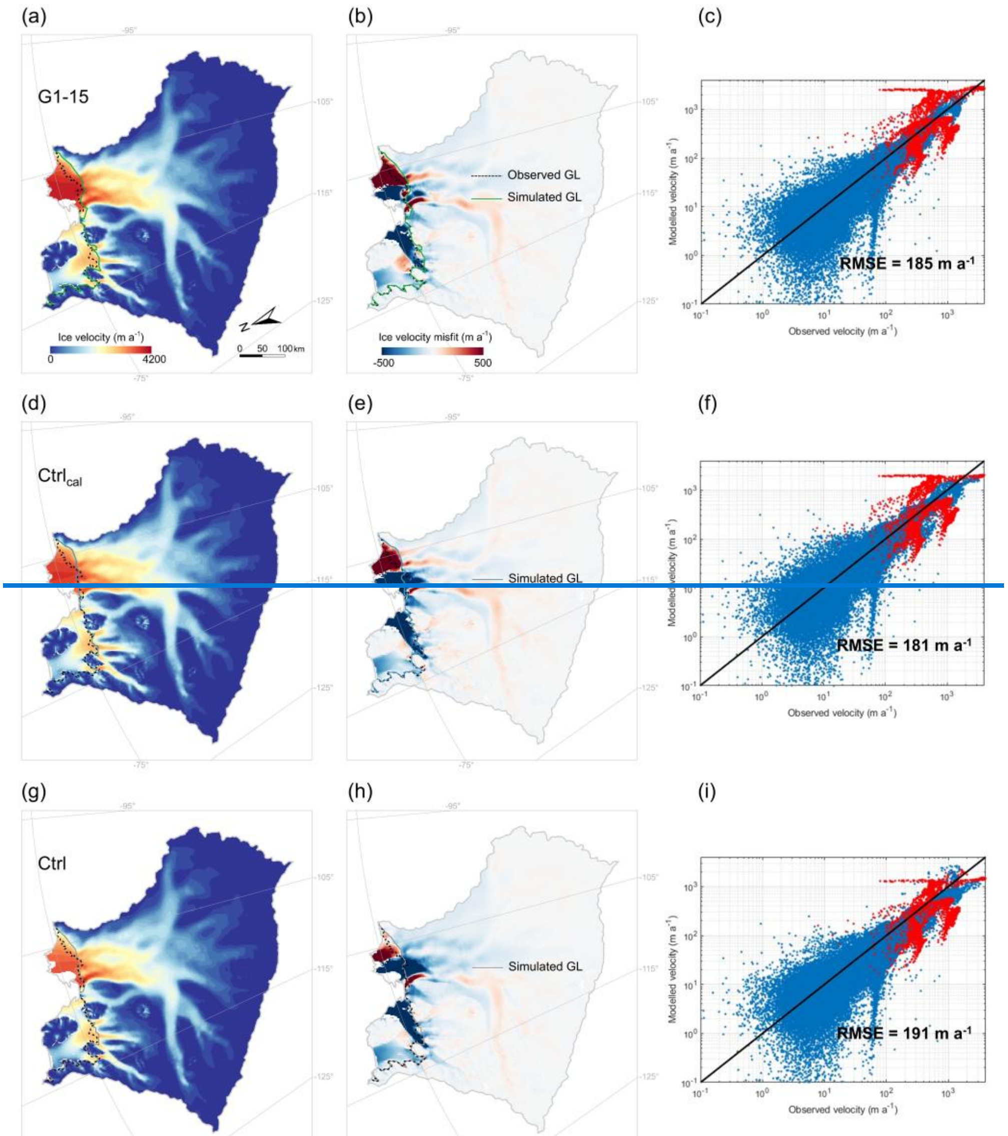

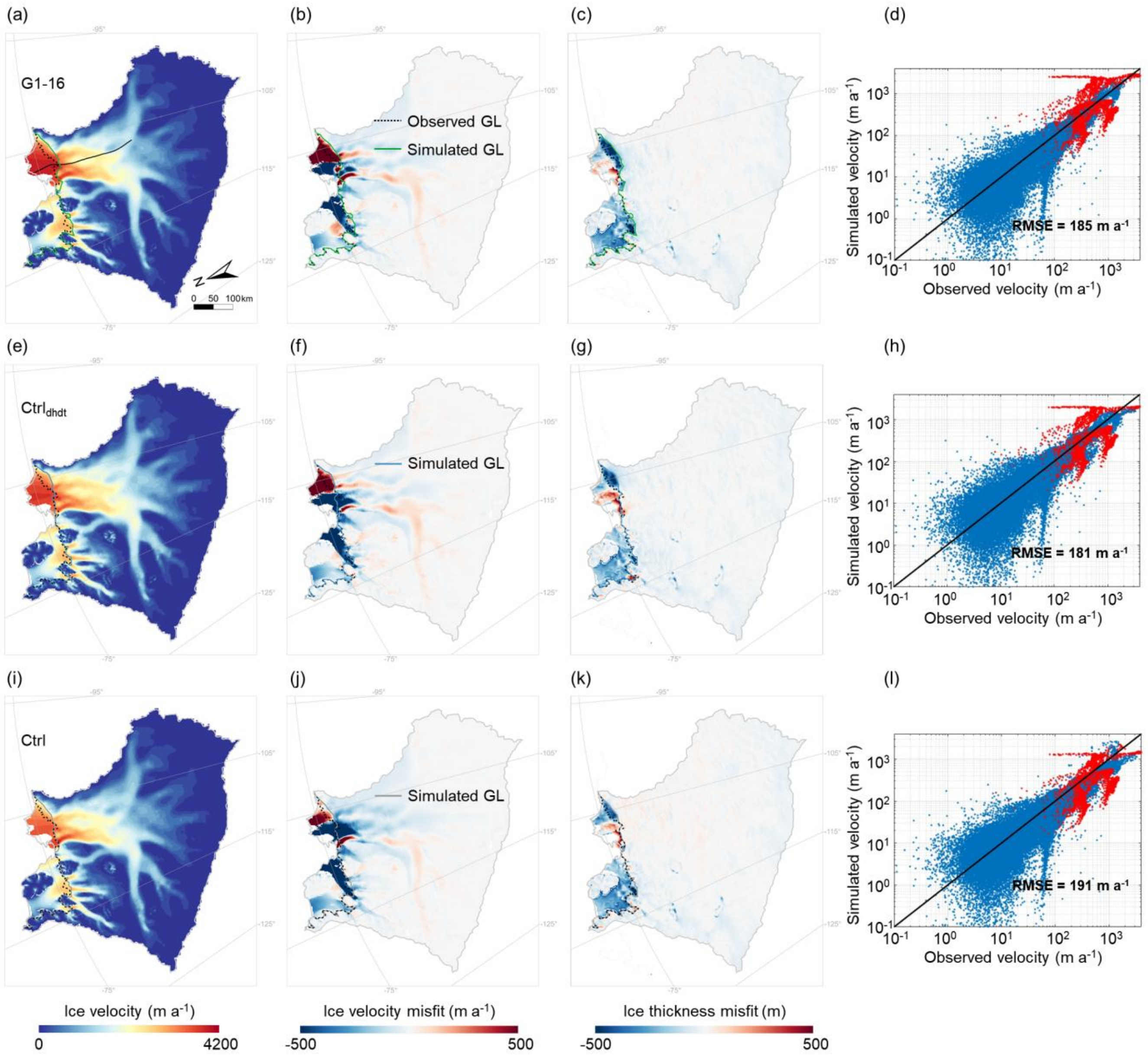

Figure ~~3. The simulated~~**4.** Simulated ice velocity and ice thickness under different simulation experiments over the historical period 1990–2020. G1-~~15~~16 denotes the simulation experiment in the ensemble of Group 1 (C_{1}~~-~~=0.23, C_{tr}~~-~~=0.26) ~~which~~that gives the most accurate (lowest RMSE) ice velocity simulation ~~result of ice velocity.~~results. The ~~Ctrl$_{cal}$~~Ctrl$_{dhdt}$ and Ctrl are the two simulation experiments ~~by~~of the model with deactivated damage processes (see ~~Methods~~Sect. 2 for details). (a), (~~d)~~e), and (~~g~~i) show the spatial distribution of simulated ice velocity in the TG basin ~~by~~of different simulation experiments. (b), (~~e)~~f), and (~~h~~j) show the difference between simulated and observed ice velocities. (c), (~~f) and (~~ig), and (k) show the difference between simulated and observed ice thickness. (d), (h) and (l) show the comparison between simulated and observed ice velocities at each grid cell in the TG basin, with blue and red dots representing the grid cells of grounded ice and floating ice, respectively. In all maps, the ~~black~~ dashed ~~line is~~black lines are the observed grounding line (Gardner et al., 2018), ~~and~~ the solid lines are the simulated grounding lines, and the light gray line is the basin boundary of the TG basin derived from Zwally et al. (2015). The solid black curve in (a) is the central flowline profile stemming from the Antarctic surface flowline dataset developed by Liu et al. (2015).~~.~~

The evolution of the vertically averaged ice damage pattern for different ensemble members is shown in Figure 5. Overall, we reproduce a widespread distribution of damage within the ice shelves of the TG basin, with lower values close to the grounding line (e.g., ranging from 0.07 for lower damage intensity to 0.24 for higher damage intensity by 2020, Figs. 5e–g) and in confined regions of the shelf. The damage fraction increases towards the ice shelf front (Fig. 5), reflecting the formation of fractures in the upstream regions – such as near the grounding line and shear margins – and their subsequent advection with ice flow. On grounded ice, damage remains low, with values generally below 0.01 across most regions. This can be attributed to the combined effects of low viscous stress and ice overburden counteracting basal crevasse formation (Sun et al., 2017). For comparison, Figure 5a presents the distribution of crevasses observed across the ice shelves of the TG basin, derived from Landsat-8 satellite images taken in December 2020. Our vertically averaged ice damage patterns tend to overestimate damage on the Dotson ice shelf, suggesting the need for a threshold stress parameter to better capture damage initiation. In contrast, ice fracture is underestimated in the Thwaites Western Glacier Tongue, likely due to the stabilizing influence of the Northwest pinning point (Surawy-Stepney et al., 2023).

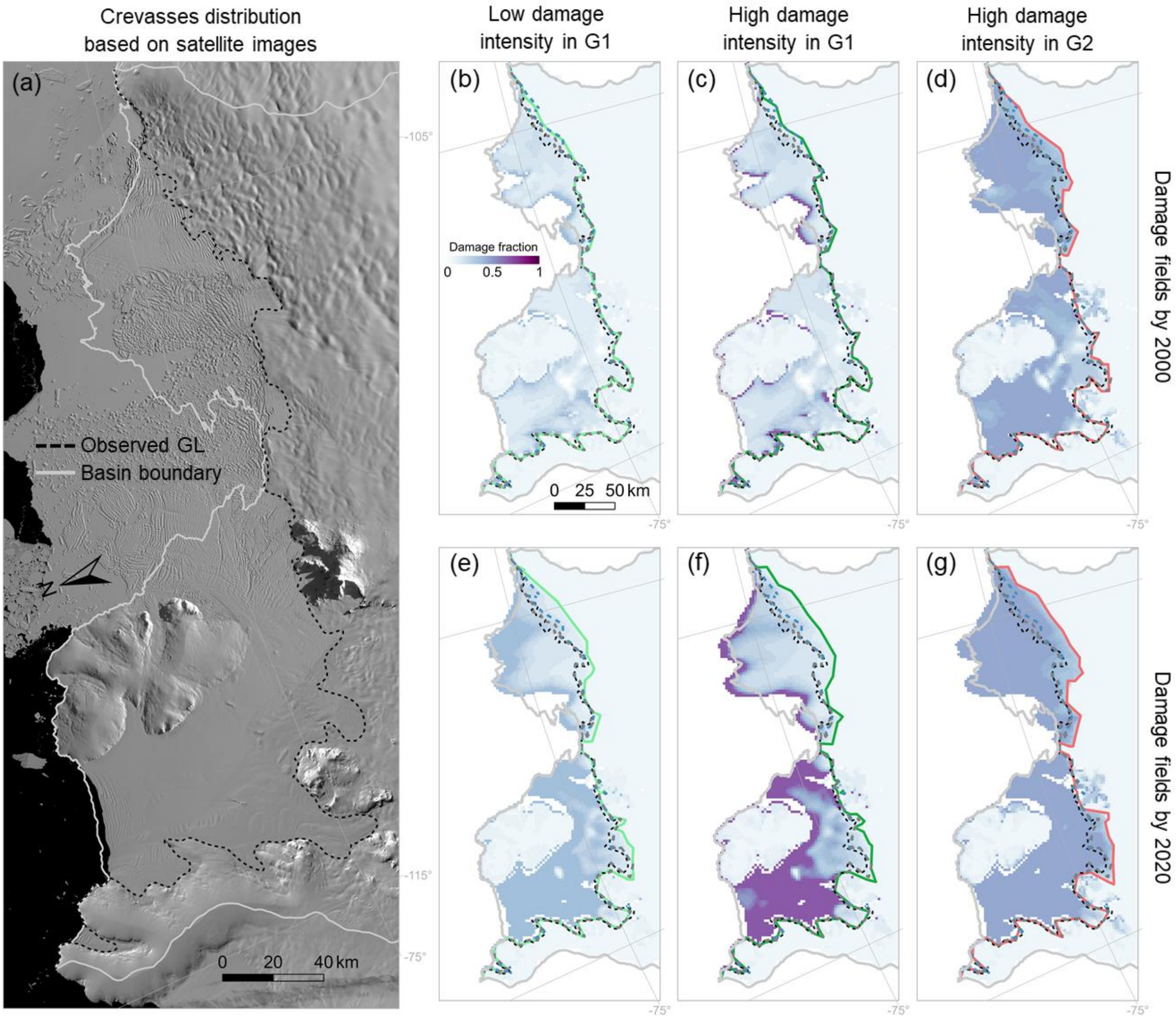

Figure 5. Damage distribution in the TG basin. (a) Observed crevasse distributions across the ice shelves of the TG basin, based on Landsat-8 satellite images acquired in December 2020. Vertically averaged damage fields (i.e., $\boldsymbol{d}(\boldsymbol{x},\boldsymbol{y})/\boldsymbol{h}(\boldsymbol{x},\boldsymbol{y})$) in the year 2000 and 2020 of the low damage intensity of Group 1 (G1) are shown in (b) and (e); the high damage intensity of G1 in (c) and (f); and the high damage intensity of Group 2 (G2) in (d) and (g). The dashed black line is the observed grounding line (Gardner et al., 2018). The light gray line is the basin boundary of the TG basin derived from Zwally et al. (2015). The dashed gray and blue lines present the initial grounding-line positions of the Ctrl/damage experiments and the Ctrl$_{dhdt}$ experiment, respectively.

3.2 ~~Effect~~Effects of ice damage on the future evolution of Thwaites Glacier

~~Comparison of projection results over the period 2020–2300 indicates~~Extending simulations to the year 2300 under constant present-day climate conditions reveals that accounting for ice damage leads to ~~an increased~~higher ice velocity, reduced ~~ice~~

~~thickness, an accelerated retreat of the grounding line, as well~~upstream ice thickness, accelerated grounding-line retreat, and greater ice mass loss compared to simulations that neglect damage processes (Figs. 6 and 7). While both G1 simulations and the Ctrl$_{dhdt}$ experiment reproduce historical mass change trends consistent with observations, they begin to diverge after approximately 15 years, around 2035. The increasing mass loss in G1 simulations suggests a positive feedback between damage processes and ice-shelf weakening in the TG basin. Ice-shelf thinning and weakening, reproduced in both experiments over the historical period (Figs. 4c and 4g), lead to increased ice velocity and decreased upstream ice thickness. In G1 simulations, this further stimulates damage formation and propagation, amplifying mass loss. Although reduced ice thickness could decrease the driving stress, potentially limiting damage formation, our model damage primarily depends on strain rates, which increase in thinning ice shelves as ~~an increased ice mass loss (Fig. 4). The~~ buttressing is reduced.

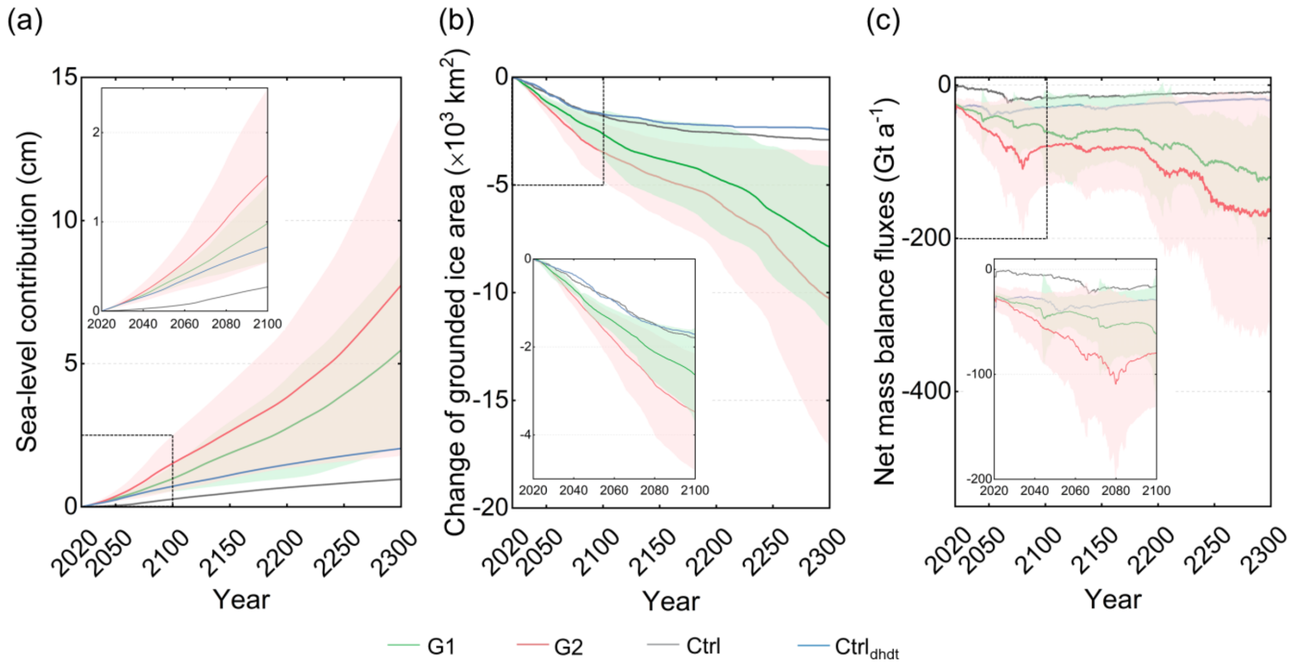

Figure 6. Evolution of (a) the simulated ~~**mean ice velocity along the central**~~contribution to sea level, (b) the change in grounded ice area, and (c) the net mass balance of the TG basin over the projection period 2020–2300 under constant present-day conditions. Note that the net mass balance does not correspond to the sum of all mass balance components (i.e., surface mass balance, sub-shelf melt, and calving fluxes); instead, it accounts for changes in the volume above flotation, which can be interpreted as the rate of mass change contributing to sea-level rise. In all panels, the solid line represents the mean, and the hatched area represents the ensemble standard deviation. The dashed black rectangular insets in each panel show the evolution of the simulation results with a focus on the period 2020–2100.

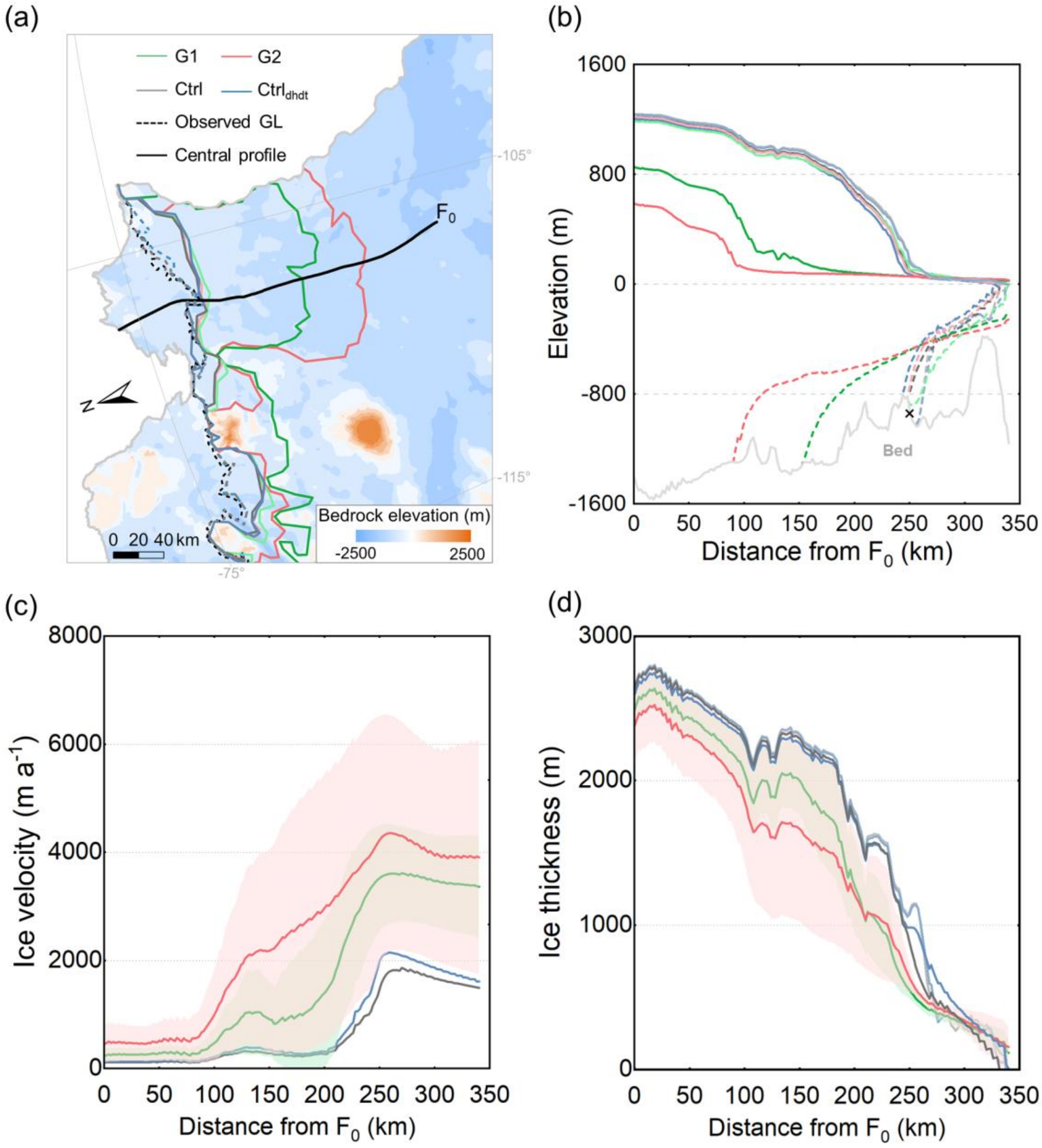

Figure 7. (a) Spatial evolution of grounding-line position. Evolution of (b) ice geometry, (c) ice velocity, and (d) ice thickness along the central flowline profile ~~**of the TG basin (the black line in Fig. 1) by simulations in Group 1 increases from 236 ± 113**~~(black curve in (a)) in TG by 2300. The light green (red) and dark green (red) lines in panels (a) and (b) represent the experiments with the least and the most retreat of the grounding line in Group 1 (Group 2), respectively, which also correspond to the experiments with the lowest and highest damage intensity in Group 1 (Group 2). The background image in panel (a) is the observed bedrock elevation of the TG basin derived from BedMachine v2 data (Morlighem et al., 2020), and the basin boundary is derived from Zwally et al. (2015). In panel (b), the dashed light gray and blue lines are the initial grounding-line positions of the Ctrl/damage experiments and the Ctrl$_{dhdt}$ experiment, and the black cross marks the location of the observed grounding line position (Gardner et al., 2018). In panels (c) and (d), the solid line represents the mean and the hatched area represents the ensemble standard deviation. The light gray and blue lines in panel (d) are the initial ice thickness along the central flowline profile of the Ctrl/damage experiments and the Ctrl$_{dhdt}$ experiment, respectively.

By 2300, the simulated mean ice mass loss in Group 1 reaches 5.5 ± 3.3 cm sea-level equivalent – 5 times higher than in the Ctrl simulations (1 cm) and more than twice that of the Ctrl$_{dhdt}$ (2 cm) experiments (Fig. 6a). Along the central flowline profile of TG (black line in Figs. 1 and 7a), the mean ice velocity in Group 1 increases from 259 ± 142 m a^{-1} for the grounded ice sheet (F$_0$) to ~~3368 ± 936~~3468 ± 986 m a^{-1} at the ice front, ~~which~~where it is ~~2–3 times of~~more than twice the ~~estimates from~~ control simulations (Fig. ~~4c). The~~ 7c). Compared to the simulated ~~mean~~initial ice thickness (light gray line in Fig. 7d), the average thinning along the central flowline profile ~~by simulations~~ in Group 1 ~~(from 2506~~is approximately 267 m ~~at inland to 108 m at ice front) is approximately 200 m thinner than the result of~~, more than five times greater than the control simulations (Fig. ~~4d).~~ 7d). As a result, the grounding line retreats further inland along a retrograde-slope bed (Figs. 7a and 7b), suggesting that the retreat may be driven by marine ice sheet instability mechanisms once the ice shelf becomes weak enough. In the case of a G1 ensemble member with high damage intensity, the grounding line retreats up to about 102 km along the central flowline profile (dark green lines in Figs. 7a and 7b), compared to the simulated initial grounding line (dashed light gray line in Fig. 7b). In contrast, in the control simulations, the grounding line remains on a bedrock ridge, limiting sustained retreat and thus enhancing stability. Ensemble members with lower damage intensities (light red and green lines in Figs. 7a and 7b) also show less retreat compared to the initial grounding line position. However, even these cases exhibit noticeable retreat across the TG basin, particularly in the upstream glacier area of TEIS.

~~With ice damage, the simulated grounding lines of TG retreat further inland than the simulation results without ice damage processes (Figs. 4a and 4b). Moreover, the simulated grounding line retreats to a retrograde-slope bed along the central profile when damage is accounted for (Fig. 4b), suggesting further inland retreat influenced by ice sheet collapse when the ice shelf becomes weak enough, indicating instability in the TG basin. In contrast, the simulated grounding lines of the control experiments are positioned at a pinning point, which is less susceptible to sustained grounding-line retreat and thus enhances their stability.~~

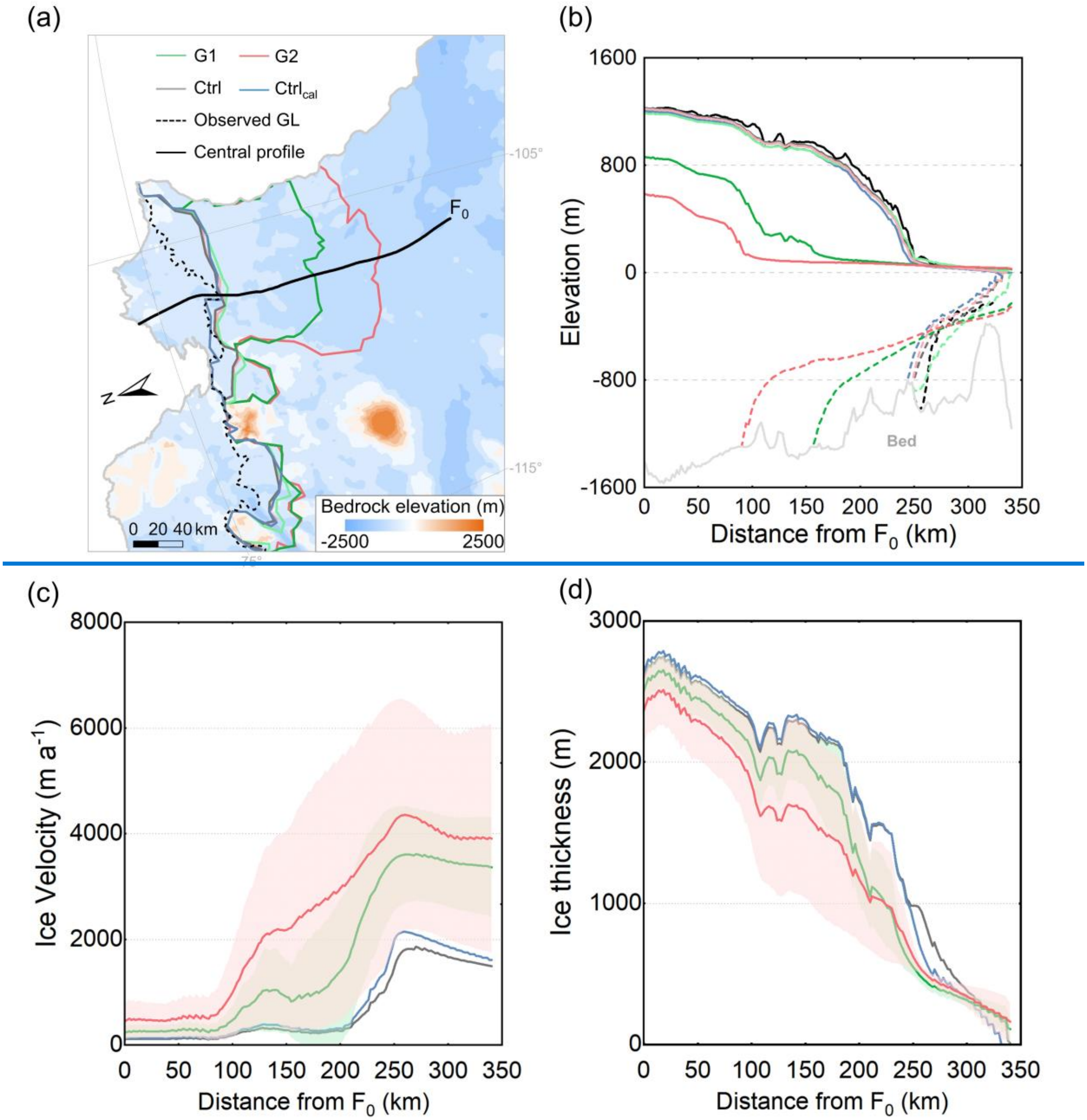

~~Figure 4. (a) Spatial evolution of grounding line position. Evolution of (b) the ice geometry, (c) ice velocity, and (d) ice thickness along the central profile (the black curve in (a)) in TG by 2300. The light green (red) and dark green (red) lines in (a) and (b) represent the experiments with the least and the most retreats of the grounding line in Group 1 (Group 2), respectively, which are also corresponding to the experiments with the lowest and highest damage strength in Group 1 (Group 2). The black dashed line presents the observed grounding line position~~ In Group 2 (high damage intensity members, Table 1), 18 out of 27 simulations resulted in model failure before 2300 (dashed dark red lines in Fig. 8a). Since the Thwaites Glacier drainage basin boundaries remain fixed, the model encounters numerical instability and eventually stops when the grounding line approaches these boundaries. This numerical failure is thus linked to basin collapse and arises from both numerical and physical instabilities. These 18 members are labeled $G2_{ext}$ (Fig. 8 and supplementary Table S1). Trends shown for G2 in Figures 6 and 7 are hence based only on the remaining 9 members. For these 9 members, the simulated mean ice mass loss reaches 1.5 cm sea-level equivalent by 2100, and 7.7 cm by 2300. In comparison, the 18 members from $G2_{ext}$ show an average ice mass loss of 7.1 ± 2.8 cm by 2100 (dark red line and hatched area in Fig. 8b), which is 7 times higher than the Group 1 mean. In the most extreme case, the grounding line retreats 128 km inland from its 2020 position along the central flowline profile within just 80 years (dark red line in Fig. 9), with an annual retreat rate 3 times higher than the most extreme case in Group 2 (light red line in Fig. 9) and 5 times higher than that in Group 1 (dark green line in Figs. 7a and 7b). By 2100, it reaches a retrograde-slope bed along the central flowline, suggesting a high potential for further inland retreat driven by marine ice sheet instability mechanisms.

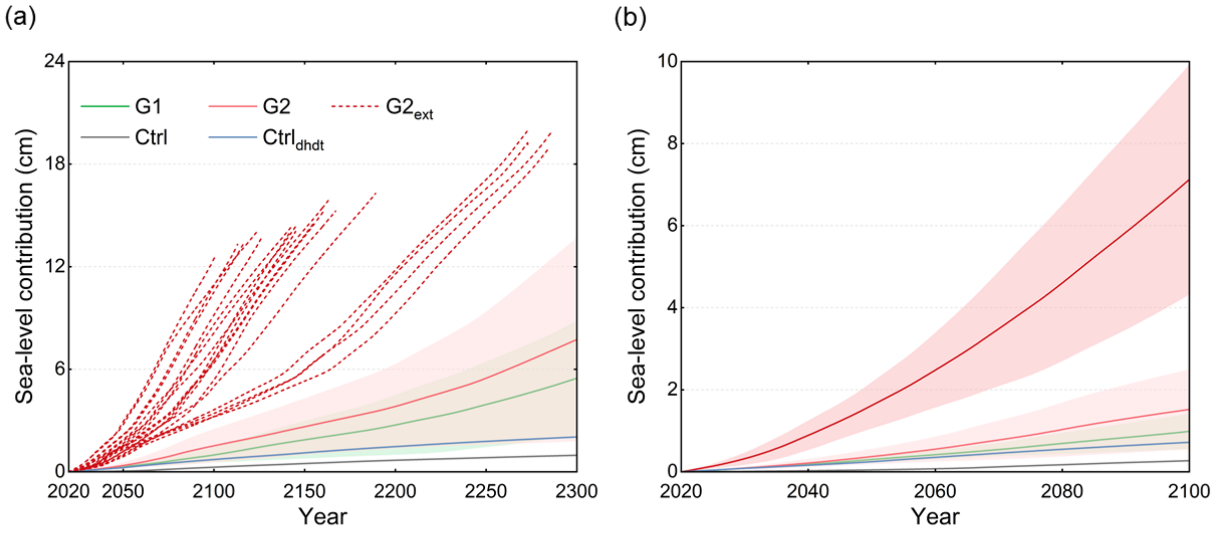

Figure 8. Evolution of the contribution of ice mass loss to sea level of the TG basin over (a) the projection period 2020–2300 and (b) with a focus on the period 2020–2100 under constant present-day conditions. The dashed red lines in panel (a) represent experiments with higher damage intensities that led to a model failure before 2300 and were grouped into Group 2 extreme experiments ($G2_{ext}$). The solid line represents the mean, and the hatched area represents the ensemble standard deviation.

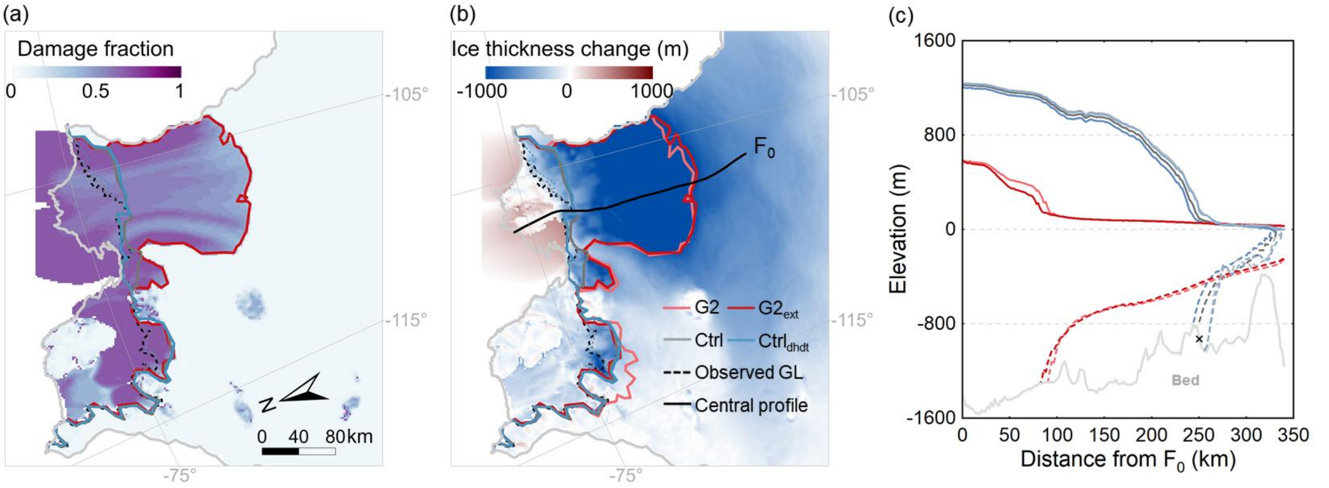

Figure 9. (a) Damage field, (b) ice thickness change, and (c) ice geometry along the central flowline profile of the simulation with the highest damage intensity in G2$_{ext}$ in the year 2100. The solid dark (light) red lines represent the spatial pattern of the ~~(Gardner et al., 2018). The background figure in (a) is the observed bedrock elevation of the TG basin derived from BedMachine v2 data (Morlighem et al., 2020). In (c) and (d), the solid line represents the mean and the hatched area represents the ensemble standard deviation. The blue and grey lines present simulated results (e.g., the simulated grounding line position, ice velocity and ice thickness) of the Ctrl$_{cal}$ and Ctrl experiments, respectively.~~

~~By 2300, the simulated mean net mass loss from simulations in Group 1 reaches -110 ± 65 Gt a^{-1}, which is 6–9 times of the estimates from control simulations (Fig. 5c). The simulated mean decrease of grounded ice area is 7243 ± 2874 km^2 compared to 2420–2904 km^2 for the simulation without ice damage (Fig. 5b). Corresponding to the increase of ice mass loss, damage processes tend to induce a larger contribution of the TG basin to global sea level rise (Fig. 5a). In year 2300, the simulated mean contribution of ice mass loss in the TG basin to global sea level rise by simulations in Group 1 is 5.0 ± 2.9 cm, higher than the simulation results from the Ctrl (1 cm) and the Ctrl$_{cal}$ (2 cm) experiments (Fig. 5a).~~

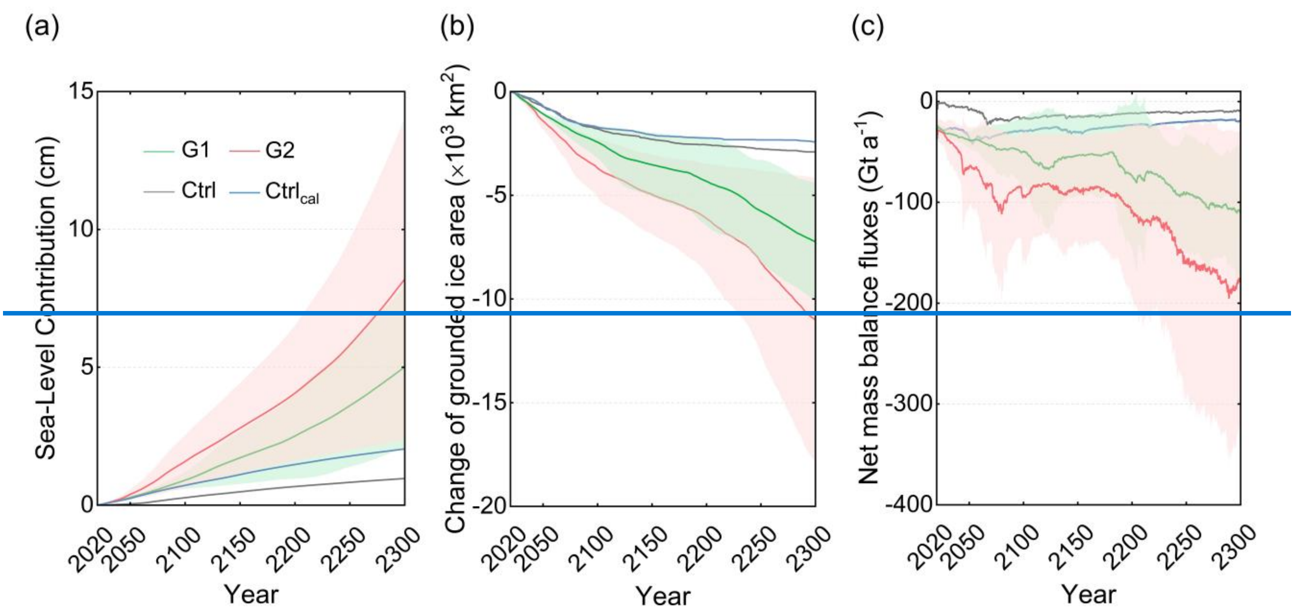

~~**Figure 5.** Evolution of (a) the contribution to global mean sea-level rise, (b) the change of grounded ice area, and (c) the net mass balance (considering volume above flotation only, i.e. the rate of mass change contributing to sea-level rise) of the TG basin over the projection period 2020–2300 under constant present-day conditions. Solid line represents mean, hatched area represents ensemble standard deviation.~~

~~**Our simulation results show the**~~ simulated grounding-line position and the ice geometry along the central flowline profile of the simulation with the highest damage intensity in $\mathrm{G2}_{\mathrm{ext}}$ (G2) in the year 2100 (2300). In panels (a) and (b), the dashed black line presents the observed grounding-line position (Gardner et al., 2018); the solid blue and gray lines present simulated grounding-line positions of the $\mathrm{Ctrl}_{\mathrm{dhdt}}$ and Ctrl experiments in 2300; the dashed gray and blue lines are the initial grounding-line positions of the Ctrl/damage experiments and the $\mathrm{Ctrl}_{\mathrm{dhdt}}$ experiment; the solid light gray line is the TG basin boundary derived from Zwally et al. (2015). In panel (c), the dashed light gray and blue lines are the initial grounding-line positions of the Ctrl/damage experiments and the $\mathrm{Ctrl}_{\mathrm{dhdt}}$ experiment, and the black cross marks the location of the observed grounding line position (Gardner et al., 2018).

Figure 10 shows the evolution of ice damage fields over time. Similar to the historical period (Fig. 5), the vertically averaged damage ($D = d/h$) fields in the ice shelf region of the Thwaites Glacier follow a pattern of increase ~~of damage fraction~~ from the grounded glacier ~~to~~toward the front of the ice shelf (Fig. ~~6~~10). Near the grounding line, the damage fraction ~~(vertically averaged damage, $D = d/h$)~~ remains relatively low ~~(~~, ranging from 0.~~1~~07 in lower~~-~~ damage ~~strength~~simulations to 0.~~4~~3 in higher~~-~~ damage ~~strength). This could be attributed to the combined effects of low viscous stress and ice overburden counteracting basal crevasse formation (Sun et al., 2017).~~simulations. As damage is ~~transported~~advected with the ice flow, this fraction increases ~~towards~~toward the ice front ~~(~~, reaching 0.3 in lower~~-~~ damage ~~strength~~cases to 0.7 in higher~~-~~ damage ~~strength),~~cases, with ~~a pronounced increase~~particularly high damage concentrated in the shear zone ~~where high damage strengths concentrate.~~

~~Moreover, our results reveal strong positive feedback between the damage processes~~. In the simulation with the highest damage intensity in $\mathrm{G2}_{\mathrm{ext}}$, the damage fraction increased from 0.4 at the grounding-line position to 0.7 at the ice front and ~~ice-shelf weakening in~~ shear margin of the TG basin ~~(Fig. 6). Damage induces ice-shelf weakening and acceleration~~ in the ~~TG~~

~~basin, which subsequently leads to ice thinning and the grounding line retreat. The increased ice velocity and decreased ice thickness further stimulate damage formation and propagation.~~year 2100 (Fig. 9a). For ~~instance,~~almost all simulations, the high damage reproduced in the ~~simulation experiment with the highest damage strength in Group 2 (right panel in Fig. 6), ice thickness declined by up to 450 m along the grounding line (Fig. 2c) and grounding-line retreats by approximately 16 km~~Dotson-Crosson area during ~~1990–2020 (Fig. 6c). By 2300, ice thickness declined by ∼1300 m around the grounding line~~ the historical period (Fig. ~~6i), and the grounding-line retreats by 148 km, along with the propagation of the damage area (Fig. 6f). A recent finding indicates that Thwaites Glacier exerts a limited~~ 5) seems to have contributed to a collapse of these ice shelves. Overall, while the buttressing effect of Thwaites Glacier's ice shelf on the upstream grounded ice may be limited (Gudmundsson et al., 2023~~). Our~~), our results suggest that ~~although~~ damage formation ~~was~~ – primarily confined to the floating ice shelf~~, the observed thinning of~~ – significantly affects the upstream grounded ice ~~sheet implies that damage on the ice shelf already impacts the upstream grounded ice, which~~and has the potential to ~~induce a remarkable retreat of the~~trigger substantial grounding line retreat in the future.

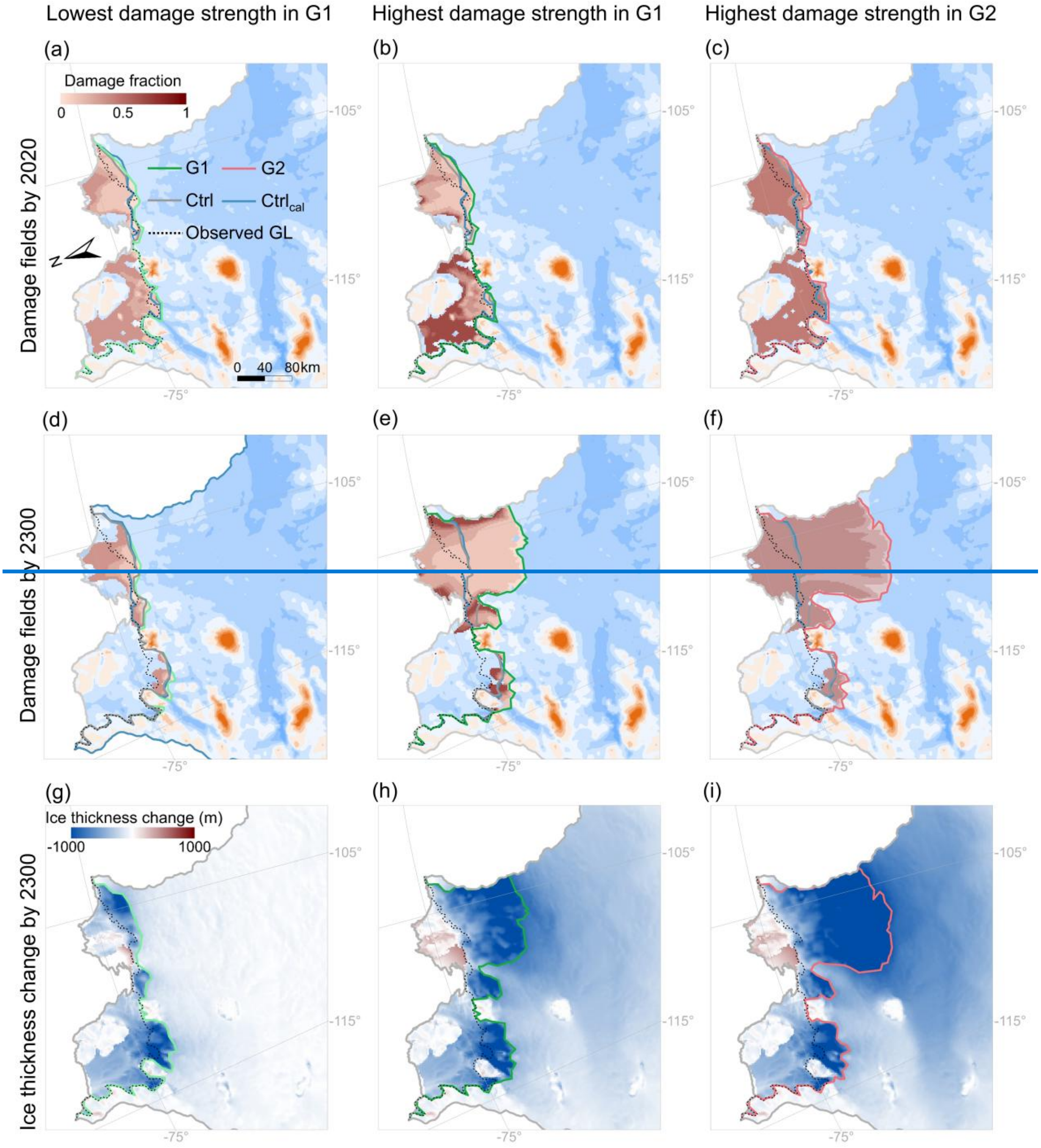
Lowest damage strength in G1
Highest damage strength in G1
Highest damage strength in G2
(a)
(b)
(c)
Damage fraction
0
0.5
1
G1
G2
Ctrl
Ctrl$_{cal}$
Observed GL
N
0 40 80km
-105°
-115°
-75°
Damage fields by 2020
(d)
(e)
(f)
Damage fields by 2300
(g)
(h)
(i)
Ice thickness change (m)
-1000
1000
Ice thickness change by 2300

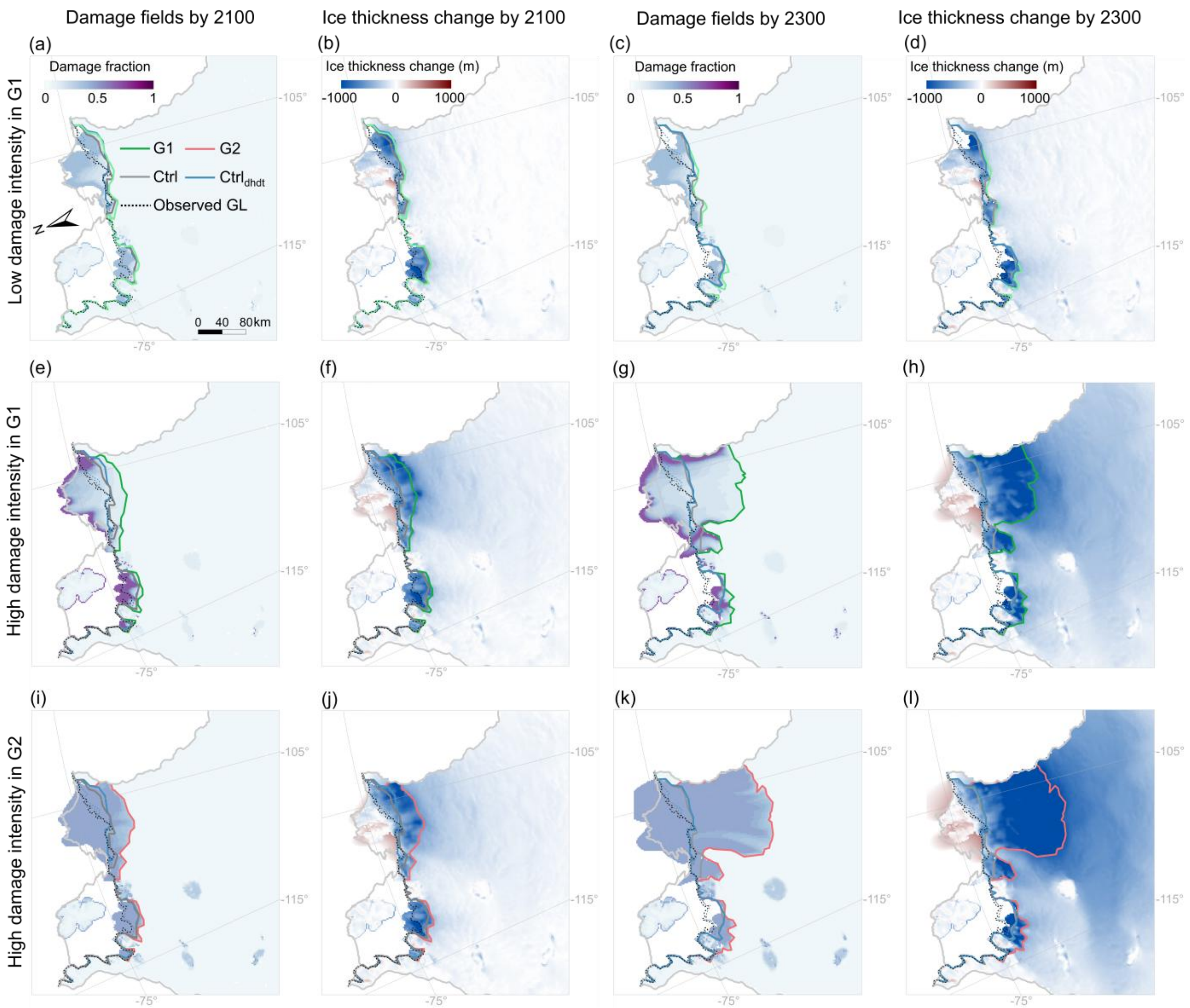

Figure ~~6. Damage~~ **10.** Vertically averaged damage fields in the year ~~2020 (the upper panel)~~2100 and 2300 ~~(the middle panel)~~ under varying damage ~~strengths~~intensities, and the ~~resulted~~resulting ice thickness change ~~(the lower panel). Maps in the first, second and third columns show simulation~~. Simulation results ~~under~~of the ~~lowest~~low damage ~~strength in~~intensity of Group 1 (G1~~), the highest damage strength in G1 and the highest~~) are shown in panels (a)–(d); the high damage ~~strength in~~ intensity of G1 in panels (e)–(h); and the high damage intensity of Group 2 (G2~~), respectively.~~) in panels (i)–(l). The ~~black~~ dashed ~~line presents~~ black lines present the observed grounding-line position (Gardner et al., 2018). The solid blue and ~~grey~~gray lines present simulated grounding-line positions ~~by~~of the ~~$\mathrm{Ctrl}_{\mathrm{cal}}$~~$\mathrm{Ctrl}_{\mathrm{dhdt}}$ and the Ctrl experiments~~, respectively.~~ in 2300. The dashed gray and blue lines are the initial grounding-line positions of the Ctrl/damage experiments and the $\mathrm{Ctrl}_{\mathrm{dhdt}}$ experiment. The solid light gray line is the TG basin boundary derived from Zwally et al. (2015).

4 Discussion

~~Previous applications of damage models on an idealized geometry created by the MISMIP+ project showed that the grounding line retreated significantly, while calving has a smaller influence on the grounding-line retreat than basal melt (Sun et al., 2017, Lhermitte et al., 2020). The strong back stress exerted by the sidewall of stat idealized basin may limit calving and the resulting ice mass loss (Sun et al., 2017). However, our simulations applied to the TG basin reveal a substantial ice mass loss due to calving, particularly under higher damage strength (Fig. A4). This finding highlights the necessity to investigate the effect of damage on ice shelves for real-world cases.~~

~~Consistent with recent observations (Rignot et al., 2019), our simulation results suggest that the ice mass loss in the TG basin is primarily driven by sub-shelf melt (Fig. A4). Sub-shelf melt thins the ice shelf, which subsequently weakens the buttressing effect of the ice shelf to the upstream grounded ice sheets, accelerating the ice flow from the upstream glacier to the ocean (Gudmundsson et al., 2019). With increasing damage, the ice mass loss caused by calving becomes a key contributor to the total ice mass loss in the TG basin (Fig. A4). By the year 2300, the mean simulated ice mass losses in the Group 1 experiments due to sub-shelf melt and calving are 129 and 106 Gt a~~$^{-1}$~~, respectively. The sum of ice mass loss caused by sub-shelf melting and calving far exceeds the ice mass accumulation on the surface of the TG, resulting in a net mass loss from the TG basin.~~

~~By arbitrarily calibrating the initial state of the TG basin using the observed mass change rates (i.e., the Ctrl~~$_{cal}$ ~~experiment), the non-damage model captures the observed ice geometry, mass balance and ice velocity in the year 2020 rather well, similar to the model with damage (Fig. 2). However, the long term projections of TG's evolution over 2020-2300 in the Ctrl~~$_{cal}$ ~~experiment differ significantly from the results simulated by the model that explicitly represents the ice damage processes. This reveals that having an accurate initial state alone is insufficient, and it is necessary to comprehensively incorporate as many key processes that affect the dynamics of glaciers and ice shelves as possible, including the ice damage, into ice-sheet models.~~

~~In addition, although the simulated historical state in the TG basin is overall consistent with observations when damage strength is properly represented in our model, there are still potential uncertainties in the projected evolution of the TG basin over 2020–2300. Firstly, we adopted the mean boundary conditions over 1995–2014 (i.e., the present-day climate condition including the surface mass balance and temperature obtained from the polar regional climate model MAR (Kittel et al., 2021) and present-day ocean temperature and salinity on the continental shelf derived from Schmidtko et al. (2014)) to initialize the model and simulate~~ Previous prognostic applications of damage models have been limited to idealized geometries, such as MISMIP+. Here, we couple the Kori-ULB ice flow model with a continuum damage mechanics framework (Sun et al., 2017) and apply it to the Thwaites Glacier basin under constant present-day climate conditions. We perform a 43-member ensemble of simulations with varying ice damage intensities and compare the results to simulations that neglect ice damage processes. When calibrated against historical satellite-derived estimates of ice mass loss from the basin, a subset of 16 ensemble members (Group 1) successfully reproduces observed ice mass loss within twice the observational uncertainty. In contrast, the control simulation without ice damage processes significantly underestimates past ice mass change. This bias can be compensated by artificially adjusting the initial state to match observed ice mass-change rates. In this adjusted experiment ($\mathrm{Ctrl_{dhdt}}$), the non-damage model reproduces the observed 2020 ice geometry, mass loss, and ice velocity comparably to the damage-inclusive model. However, mass loss projections for 2020–2300 in the $\mathrm{Ctrl_{dhdt}}$ experiment diverge significantly from those that explicitly represent ice damage processes. Specifically, simulations accounting for ice damage predict more than twice the ice mass loss, higher mean ice velocity along the central flowline profile, and greater inland retreat of the grounding line (Figs. 6 and 7). This suggests a positive feedback between damage processes and ice-shelf weakening in the TG basin. Overall, our results show that increasing damage intensity leads to higher ice velocities, accelerated glacier retreat and greater ice mass loss, underlining the importance of accounting for damage feedbacks in ice-sheet projections.

However, it is important to acknowledge that the application of prognostic modeling to assess the impact of ice damage on the dynamic evolution of ice shelves remains very preliminary. Comparison between simulated vertically integrated damage fields over the historical ~~and future evolution of the TG basin. These boundary conditions do not necessarily represent the real imbalance of the ice sheet for that~~ period~~. Secondly, we did not account for~~ and observed crevasse distributions shows inconsistencies, with damage projections not consistently matching observed patterns (Fig. 5). Our approach has the benefit of using a physical approach to infer crevasse formation. However, direct comparison with observation remains challenging, since the damage field is highly variable and corresponds to a particular time moment. Our results are highly dependent on the forcing and model uncertainties, which makes a direct comparison unfeasible. Moreover, modeled damage patterns are highly variable across ensemble members. These discrepancies may be explained by the limitations of the damage model. For example, our approach does not account for all mechanisms of damage healing, which may result in an overestimation of ~~the damage field (Sun et al., 2017). Previous studies have found that crevasses can be healed, in response to overburden pressure, surface ice accumulation, and refreezing (Albrecht and Levermann, 2012; Surawy-Stepney et al., 2023b). Dense crevasses near the grounding zone can be healed during their advection towards the calving front. The~~damage (Sun et al., 2017). In reality, crevasse healing ~~process of crevasses~~ can occur when ~~shearing~~shear stress along the flow path decreases notably (Wesche et al., 2013; Benn and Åström, 2018~~). However,~~), and dense crevasses near the grounding zone may heal during their advection towards the calving front. However, studies on the process of ice healing are still scarce due to the challenges ~~in~~of monitoring and quantifying this process (Albrecht and Levermann, 2012). Additionally, a vertically-integrated model may not be appropriate for accurately representing crevasse formation mechanisms. The application of threshold stress for damage initiation as well as mechanisms of crevasse healing, such as the accretion of marine ice within basal crevasses, should be explored (Sun et al., 2017). The lack of representation of plastic necking (Bassis and Ma, 2015) also introduces uncertainties in our results. While the comparison of modeled, vertically integrated damage fields with snapshots of surface crevasses is not straightforward, these discrepancies underline the need for further validation and calibration of the damage model. Instead of solely relying on ice sheet mass loss data, future efforts should incorporate observational datasets of crevasse distributions. Moreover, while the simulated historical state of the TG basin is overall consistent with observations, the 1995–2014 mean boundary conditions used to initialize the model and simulate hindcasts for 1990–2020 (Schimdtko et al., 2014; Kittel et al., 2021) do not necessarily reflect the actual imbalance of the ice sheet during that period.

This study focuses specifically on damage and its influence on ~~the~~ ice~~-~~-sheet stability~~,~~ but ignores the potential ~~effect~~effects of hydrofracturing and marine ice-cliff instability (MICI). Previous studies have shown that hydrofracturing resulting from surface melting plays a ~~vital~~crucial role in ice-shelf disintegration (Bassis and Walker, 2012; DeConto and Pollard, 2016; Bassis et al., 2021; Laffin et al., 2022~~, Bassis and Walker, 2012, Bassis et al., 2021).~~). Pollard et al. (2015) found that the combined mechanisms of MISI, hydrofracturing and MICI can drastically accelerate the collapse of the West Antarctic Ice Sheet~~ in several~~, potentially within decades~~ (Pollard et al., 2015).~~, under a Pliocene-like warming scenario. Similar to Sun et al. (2017), the CDM framework used in ~~this~~the present study only considers dry crevasses~~,~~, and hence ignores hydrofracturing. This may result in an underestimation of ice velocity and ice mass loss from the TG basin in our ~~simulation results.~~simulations. However, recent studies suggest that Thwaites Glacier ~~might~~may be less vulnerable to MICI than previously thought~~, and~~. Instead, the intrusion of warm seawater or ice~~-~~-sheet surface melt could substantially enhance the response of marine ice sheets to climate change by increasing melting and slipperiness (Morlighem et al., 2024; Robel, 2024). This increased melting can, in turn, lead to substantial ice damage. Our results ~~also indicate~~suggest that ice damage could be ~~an alternative process to explain the rapid ice loss~~a key driver of Thwaites Glacier~~. Furthermore, the lack of representation of some other processes, such as basal hydrological processes, the accretion of marine ice within basal crevasses (Sun et al., 2017) and plastic necking (Bassis and Ma, 2015), is also potential to induce some uncertainties in our simulation results.~~

’s rapid ice loss, offering an alternative explanation to previous hypotheses.

Our study focuses exclusively ~~investigates~~on the sensitivity of ice dynamics (e.g., ~~the~~ grounding-line retreat, ice velocity, and ice thickness) and ice mass change in the TG basin to ~~the~~ damage ~~strength. Nevertheless,~~intensity. It should be noted that these findings may not hold true in other basins in Antarctica. ~~Thus, it is necessary to apply our model to more basins with different climatic, geometrical and oceanic conditions. Moreover, it~~Further simulations across various glaciers and ice shelves are needed to assess the robustness of ice-sheet models incorporating ice damage processes. It is also important to investigate the ~~influence~~impact of ice damage on the evolution of the ~~Antarctic ice sheet~~AIS under different climate change scenarios (Seroussi et al., 2020). ~~Such a~~A comprehensive ~~study is vital~~understanding of these processes is key for ~~accurately predicting~~improving projections of the future evolution of the ~~Antarctic ice sheet~~AIS and its contribution to global sea-level rise under climate change.

5 Conclusion

In this study, we performed a comprehensive analysis ~~on~~of the response of the Thwaites Glacier to varying intensities of ice damage ~~at different strengths~~ using the Kori-ULB ice-sheet model~~. Comparison of simulation results from the model~~ coupled with ~~activated and deactivated~~a continuum damage mechanics model. By calibrating our simulations with satellite-based observations, we show that explicitly representing ice damage processes ~~indicates that an explicit representation of ice damage~~

~~in the ice-sheet~~ improves the model~~ allows~~'s ability to ~~better simulate~~capture the observed ice ~~geometry and~~ mass ~~balance~~change in the ~~Thwaites Glacier~~TG basin~~.~~ compared to the default model without damage. Even when starting from a present-day state ~~calibrated against~~artificially adjusted to match observed ice mass~~-~~ change rates, ~~the projection~~projections of ~~the~~ Thwaites Glacier ~~basin's evolution from 2020 to 2300 without~~that neglect ice damage ~~differs~~diverge significantly from ~~simulations~~those that ~~explicitly represent the ice~~include it, suggesting a positive feedback between damage processes~~.~~ ~~Increased damage strength generally~~ and ice-shelf weakening in the TG basin. Overall, our results demonstrate that increasing damage intensity results in ~~larger retreat of the grounding line,~~ higher ice ~~velocity, thinner ice shelves, more~~velocities, accelerated glacier retreat and greater ice mass loss, ~~and bigger contribution to global sea-level rise.~~emphasizing the importance of accounting for damage feedbacks in ice-sheet projections. This study highlights the ~~necessity~~need for further research on ice damage processes ~~and the importance of integrating damage into ice-sheet models~~ to ~~more accurately project~~improve projections of the future evolution of the Antarctic ice sheet under climate change.

Code and data availability. The code and reference manual of the Kori-ULB ice-sheet model are publicly available on GitHub via https://github.com/FrankPat/Kori-dev (last access: 9 September 2024). The ~~specific Kori-ULB~~ model version and simulation results used in this study~~, the simulation outputs will be made~~ are available on Zenodo ~~once published.~~(https://zenodo.org/records/15114549). All datasets used in this study are freely accessible through their original references. The MAR outputs used in this study are available on Zenodo (https://doi.org/10.5281/zenodo.4459259; Kittel et al., 2021).

Author contributions. YL conceived the study in collaboration with VC, JB, GQ, QY and FP. YL and VC developed the experimental setup and design, with contributions from JB and FP. YL set up the ice-sheet model and performed all model simulations. YL performed the data analysis, produced the figures, and wrote the original manuscript draft. All authors contributed to designing the simulations and provided feedback on the analysis and input to the manuscript.

Competing interests. The authors declare that they have no conflict of interest.

Acknowledgements. YL and QY received support from the National Natural Science Fund of China (No. 42406242), the Southern Marine Science and Engineering Guangdong Laboratory (Zhuhai) (Nos. SL2021SP201 and SML2022SP401), and the Fundamental Research Funds for the Central Universities, Sun Yat-sen University (No.74110-31610046). This research was also supported by OCEAN:ICE~~,~~ (which is co-funded by the European Union, Horizon Europe Funding Programme for research and innovation under grant agreement Nr. 101060452 and by UK Research and Innovation~~. O:I Contribution number XX.~~) and the HiRISE (NWP GROOT, Netherlands, under grant agreement No. OCENW.GROOT.2019.091). Computational resources have been provided by the Consortium des Équipements de Calcul Intensif (CÉCI), funded by the Fonds de la Recherche Scientifique de Belgique (F.R.S.-FNRS) under Grant No. 2.5020.11 and by the Walloon Region.~~ JB received~~

~~support from the HiRISE (NWP GROOT, Netherlands) under grant agreement No. XX and the Nederlandse Organisatie voor Wetenschappelijk Onderzoek (NWO) under grant No. OCENW.GROOT.2019.091.~~

~~Appendix A: Integration of the CDM model into the Kori-ULB ice-sheet numerical model~~

~~We implement the CDM in the Kori-ULB ice sheet numerical model. In Kori-ULB, the relationship between the deviatoric stress τ and the strain rate $\dot{\varepsilon}$ is described by Glen's constitutive flow law:~~

~~$2A\tau^2\tau = \dot{\varepsilon}$, (A1)~~

~~A is Glen's flow law factor. Following Sun et al., (2017) and Bassis and Ma (2015) the propagation of damage reduces the ice viscosity, through Glen's flow law, leading to faster ice flow. Here, a damage factor $D(\tau)$ is introduced in Eq. (A1) to describe this damage feedback process in Kori-ULB:~~

~~$2A\tau^2\tau = (1 - D(\tau))^3$, (A2)~~

~~Given the shallow shelf approximation, this results in the following expression for the vertically integrated effective viscosity:~~

~~$2h\mu = (h - \tau_1)A^{-\frac{1}{3}}\dot{\varepsilon}^{-\frac{2}{3}}$, (A3)~~

~~where, μ is effective viscosity and h is ice thickness. In Kori-ULB, the first principal stress τ_1 and ice velocity $v = (u, v)$ together can be numerically solved using the stress balance equation. In this way, the relationship between the damage and the first principal stress τ_1 needs to be defined to realize the coupling of the damage with the Kori-ULB ice sheet model. Here, we use CDM to link the damage and τ_1. CDM considers both the local source of damage and its transport during ice flow (Sun et al., 2017). The local source of damage can be described by the total depth of the crevasses (Nick et al., 2011, 2013; Cook et al., 2014), which includes the depth of surface crevasses d_s and the depth of basal crevasses d_b, and can be calculated by the zero-stress rule (Nye, 1957; Nick et al., 2011):~~

~~$d_s = \frac{\tau_1}{\rho_i g} + \frac{\rho_w}{\rho_i} d_w$, (A4)~~

~~$d_b = \frac{\rho_i}{\rho_w - \rho_i}\left(\frac{\tau_1}{\rho_i g} - H_{ab}\right)$, (A5)~~

~~where, d_w is the water depth in the surface crevasse (here we only consider dry crevasses, so $d_w = 0$), H_{ab} is the thickness above floatation, $g = 9.81$ m s^{-2} is the gravitational acceleration, $\rho_i = 917$ kg m^{-3} and $\rho_w = 1028$ kg m^{-3} are the ice and seawater density, respectively. τ_1 can be calculated by the principal strain ε:~~

~~$\tau_1 = \frac{1}{2}\,\varepsilon\,\mu$, (A6)~~

~~Then, the total local crevasse depth, namely the local damage $d_1(\tau_1)$ can be defined as:~~

~~$d_1(\tau_1) = max\ (0, \left((d_s, d_s + d_b)\ , C_1 * h\right)\ )$,~~ ~~(A7)~~

~~Here, we use damage parameter C_1 to describe the upper limit of the local damage $d_1(\tau_1)$ as a fraction of the ice thickness, with the parameter ranging from 0 to 1. If there is no advection, τ_1 can be determined by setting it equal to the overall depth of crevasses.~~

~~The damage transport during ice flow describes the evolution of the damage field due to advection, stretching, and the loss and accumulation of mass on the upper and lower surfaces of the glacier. For any time and position (x, y, t), there is a local damage field d_1(x, y, t) and a transport damage field d_{tr}(x, y, t), the latter describes the total depth of crevasses after the ice flow process by solving the damage transport equation (Sun et al., 2017):~~

~~$\frac{\partial d_{tr}}{\partial t} + \nabla \cdot (u d_{tr}) = -[(\dot{a}, 0)\ + (\dot{m}, 0)\,] \frac{d_{tr}}{h}$,~~ ~~(A8)~~

~~The left-hand side of Eq. (A8) represents the vertically integrated damage conservation under ice flow, which includes the movement of the crevasses along with the ice flow and the stretching and compression. On the right-hand side, an increase in undamaged ice thickness is presumed to occur due to accumulation on the upper surface ($\dot{a}$), while the crevassed underside is eroded by basal melting ($\dot{m}$). Regardless of whether the horizontal flow field is divergent or convergent, all these factors maintain a constant ratio of d_{tr} to h (Sun et al., 2017).~~

~~Assuming that at least during the timescale of the closure process, the crevasse surfaces do not bond together as a result of crevasse closure, the final relationship $d(\tau_1)$ is expressed as:~~

~~$d(\tau_1) = min(C_{tr} * h, max\ (d_1(\tau_1), d_{tr}))$,~~ ~~(A9)~~

~~By bringing Eq. (A7) into Eq. (A9):~~

~~$d(\tau_1) = min\left(C_{tr} * h, max\ \left(\left(0, \left((d_s, d_s + d_b)\ , C_1 * h\right)\right)\ , d_{tr}\right)\right)$,~~ ~~(A10)~~

~~Here, the damage parameter C_{tr} describes the upper limit of $d(\tau_1)$ as a fraction of the ice thickness (with the parameter ranging from 0 to 1), and C_1 is equal to or less than C_{tr}.~~

~~Appendix B: Evolution of the Thwaites Glacier basin by a snapshot in 2100~~

~~In Group 2, 18 samples of the parameters C_1 and C_{tr}, which represent a very high damage strength, triggered a model collapse before 2300 (Table A1). Here, we grouped these experiments into Group 2 extreme experiments ($G2_{ext}$) (Fig. A5a). These higher damage strengths in $G2_{ext}$ averagely resulted in a contribution to global mean sea level rise of 7.1 ± 2.8 cm by 2100 (the dark red line and its hatched area in Fig. A5b), which is eight times of the mean prediction from the simulations of Group 1. In the simulation with the highest damage strength in $G2_{ext}$, the damage fraction increased from 0.4 at the grounding-line position to 0.7 at the ice front and shear margin of the TG basin in the year 2100 (Figs. A6a). The grounding line retreated by 128 km inland from its position in the year 2020 over a period of only 80 years. The mean annual retreat rate is more than~~

~~three times of the mean retreat rate simulated by Group 2 experiments and even more than five times of the mean retreat rate simulated by Group 1 experiments (Figs. A6b–A6c). Moreover, the simulated grounding line of the experiment with the highest damage strength in G2$_{ext}$ retreats to a retrograde-slope bed along the central flowline profile in the year 2100, indicating a high potential to retreat further toward inland due to the impact of ice sheet collapse.~~

~~**Table A1.** Summary of the damage sensitivity experiments and two control experiments performed at the TG basin under constant present-day conditions. The values of parameters C_1 and C_{tr} of the 43 simulations considering the damage processes are produced using Latin hypercube sampling in their parameters space.~~

~~**Scenarios**~~	~~**ID**~~	~~**Damage parameters**~~		~~**Forward simulation type**~~		~~**RMSEs over 1990-2020**~~		
		~~C_1~~	~~C_{tr}~~	~~Historical simulation~~	~~Extended simulation~~	~~RMSE (whole basin)~~	~~RMSE (floating ice)~~	~~RMSE (grounded ice)~~
~~Ctrl~~ ~~deactivated damage processes~~		~~-~~	~~-~~	~~1990-2020~~	~~2300~~	~~190.9~~	~~745.2~~	~~95.6~~
~~Ctrl$_{cal}$~~ ~~deactivated damage processes~~ ~~&~~ ~~satellite-observed mass balance calibrated (Otosaka et al., 2023)~~		~~-~~	~~-~~	~~1990-2020~~	~~2300~~	~~181.3~~	~~752.7~~	~~71.0~~
	~~1~~	~~0.0576~~	~~0.7712~~	~~1990-2020~~	~~2300~~	~~327.7~~	~~1394.3~~	~~67.1~~

~~Group 1 damage processes & SLC and net mass balance within the range of observational estimates ± 2 s.d. (0.24 ± 0.08 cm and -46.1 ± 14.4 Gt a^{-1}) in the historical simulation (Shepherd et al., 2019)~~	~~2~~	~~0.0585~~	~~0.5215~~	~~1990-2020~~	~~2300~~	~~221.1~~	~~928.1~~	~~62.5~~
	~~3~~	~~0.0657~~	~~0.3400~~	~~1990-2020~~	~~2300~~	~~196.8~~	~~815.0~~	~~63.6~~
	~~4~~	~~0.0806~~	~~0.6590~~	~~1990-2020~~	~~2300~~	~~271.4~~	~~1137.4~~	~~65.4~~
	~~5~~	~~0.0838~~	~~0.5067~~	~~1990-2020~~	~~2300~~	~~233.0~~	~~974.2~~	~~63.4~~
	~~6~~	~~0.0909~~	~~0.3521~~	~~1990-2020~~	~~2300~~	~~194.8~~	~~805.4~~	~~60.4~~
	~~7~~	~~0.0951~~	~~0.5530~~	~~1990-2020~~	~~2300~~	~~249.4~~	~~1041.0~~	~~63.9~~
	~~8~~	~~0.1014~~	~~0.3265~~	~~1990-2020~~	~~2300~~	~~192.3~~	~~794.2~~	~~60.2~~
	~~9~~	~~0.1297~~	~~0.3007~~	~~1990-2020~~	~~2300~~	~~192.3~~	~~791.1~~	~~59.2~~
	~~10~~	~~0.1385~~	~~0.4258~~	~~1990-2020~~	~~2300~~	~~234.3~~	~~967.1~~	~~62.8~~
	~~11~~	~~0.1399~~	~~0.2846~~	~~1990-2020~~	~~2300~~	~~189.4~~	~~776.2~~	~~59.7~~
	~~12~~	~~0.1780~~	~~0.2613~~	~~1990-2020~~	~~2300~~	~~185.9~~	~~760.0~~	~~60.2~~
	~~13~~	~~0.1819~~	~~0.2600~~	~~1990-2020~~	~~2300~~	~~185.6~~	~~757.8~~	~~60.3~~
	~~14~~	~~0.1932~~	~~0.2591~~	~~1990-2020~~	~~2300~~	~~185.2~~	~~756.2~~	~~60.2~~
	~~15~~	~~0.2255~~	~~0.2588~~	~~1990-2020~~	~~2300~~	~~184.9~~	~~754.4~~	~~59.9~~
~~Group 2: damage processes & SLC and net mass balance outside the range of observational estimates ± 2 s.d. in the historical simulation~~	~~1~~	~~0.0174~~	~~0.9257~~	~~1990-2020~~	~~2300~~	~~178.8~~	~~709.7~~	~~77.6~~
	~~2~~	~~0.0249~~	~~0.1666~~	~~1990-2020~~	~~2300~~	~~181.1~~	~~705.8~~	~~87.3~~
	~~3~~	~~0.0308~~	~~0.9861~~	~~1990-2020~~	~~2300~~	~~606.6~~	~~2468.7~~	~~77.8~~
	~~4~~	~~0.0429~~	~~0.3302~~	~~1990-2020~~	~~2300~~	~~193.2~~	~~795.9~~	~~67.3~~
	~~5~~	~~0.0682~~	~~0.9409~~	~~1990-2020~~	~~2273~~	~~560.8~~	~~2217~~	~~106.7~~
	~~6~~	~~0.0778~~	~~0.1783~~	~~1990-2020~~	~~2300~~	~~184.1~~	~~755.1~~	~~64.8~~
	~~7~~	~~0.1232~~	~~0.9702~~	~~1990-2020~~	~~2145~~	~~1092~~	~~3962.9~~	~~260.8~~
	~~8~~	~~0.1381~~	~~0.8655~~	~~1990-2020~~	~~2164~~	~~554.8~~	~~2134.1~~	~~128.5~~
	~~9~~	~~0.1486~~	~~0.6384~~	~~1990-2020~~	~~2286~~	~~489.8~~	~~1980.6~~	~~104.6~~
	~~10~~	~~0.1579~~	~~0.5134~~	~~1990-2020~~	~~2300~~	~~270~~	~~1114.8~~	~~63~~
	~~11~~	~~0.1759~~	~~0.8237~~	~~1990-2020~~	~~2160~~	~~427.3~~	~~1603~~	~~126.6~~
	~~12~~	~~0.1807~~	~~0.4473~~	~~1990-2020~~	~~2300~~	~~253.3~~	~~1043.6~~	~~63.1~~
	~~13~~	~~0.1911~~	~~0.6941~~	~~1990-2020~~	~~2189~~	~~404.2~~	~~1586.3~~	~~102.6~~
	~~14~~	~~0.2267~~	~~0.7377~~	~~1990-2020~~	~~2155~~	~~403~~	~~1508.7~~	~~123.9~~
	~~15~~	~~0.2335~~	~~0.3962~~	~~1990-2020~~	~~2300~~	~~246.7~~	~~1015~~	~~62.9~~
	~~16~~	~~0.2411~~	~~0.4244~~	~~1990-2020~~	~~2300~~	~~301.7~~	~~1246.1~~	~~67.3~~
	~~17~~	~~0.2604~~	~~0.467~~	~~1990-2020~~	~~2284~~	~~512.1~~	~~2076.9~~	~~112.1~~
	~~18~~	~~0.2812~~	~~0.3218~~	~~1990-2020~~	~~2300~~	~~212.7~~	~~868.6~~	~~62~~
	~~19~~	~~0.3068~~	~~0.648~~	~~1990-2020~~	~~2146~~	~~359.8~~	~~1334.9~~	~~124.1~~
	~~20~~	~~0.3497~~	~~0.6175~~	~~1990-2020~~	~~2126~~	~~552.9~~	~~2057.9~~	~~165.6~~
	~~21~~	~~0.3674~~	~~0.6608~~	~~1990-2020~~	~~2101~~	~~1186.3~~	~~4249.6~~	~~301.6~~
	~~22~~	~~0.3789~~	~~0.4358~~	~~1990-2020~~	~~2273~~	~~526.8~~	~~2140.1~~	~~118.2~~
	~~23~~	~~0.3877~~	~~0.6057~~	~~1990-2020~~	~~2113~~	~~622.4~~	~~2291~~	~~190.8~~
	~~24~~	~~0.4129~~	~~0.5769~~	~~1990-2020~~	~~2116~~	~~574~~	~~2140.6~~	~~183.5~~
	~~25~~	~~0.428~~	~~0.5242~~	~~1990-2020~~	~~2167~~	~~273.4~~	~~1018.8~~	~~109.9~~
	~~26~~	~~0.4538~~	~~0.5433~~	~~1990-2020~~	~~2143~~	~~289.8~~	~~1075.1~~	~~112.1~~
	~~27~~	~~0.4711~~	~~0.5318~~	~~1990-2020~~	~~2142~~	~~262~~	~~983.3~~	~~100.3~~
	~~28~~	~~0.5202~~	~~0.5657~~	~~1990-2020~~	~~2124~~	~~624~~	~~2330.4~~	~~192.7~~

~~**Table A2.** Summary of the forcing and model calibration and evaluation data used in this study.~~

~~**Data type**~~	~~**Study**~~	~~**Period**~~	~~**Value**~~
~~Present-day SMB and temperature (MARv3.11)~~	~~Kittel et al., 2021~~	~~1995-2014~~	~~–~~

~~Present-day ocean temperature and salinity~~	~~Schmidtko et al., 2014~~	~~1975-2012~~	~~–~~
~~Contribution of the TG basin to Sea-level rise~~	~~Shepherd et al., 2019~~	~~1992–2017~~	~~0.24 ± 0.08 cm~~ ~~(mean ± 2 s.d.)~~
~~Net mass balance of the TG basin~~	~~Shepherd et al., 2019~~	~~1992–2017~~	~~-46.1 ± 14.4 Gt a^{-1}~~ ~~(mean ± 2 s.d.)~~
~~MEaSUREs InSAR-Based Antarctica Ice Velocity Map, Version 2~~	~~Rignot et al., 2017~~	~~1996–2016~~	~~–~~
~~Surface elevation change of the Amundsen Sea Embayment~~	~~Otosaka et al., 2023~~	~~1992–2019~~	

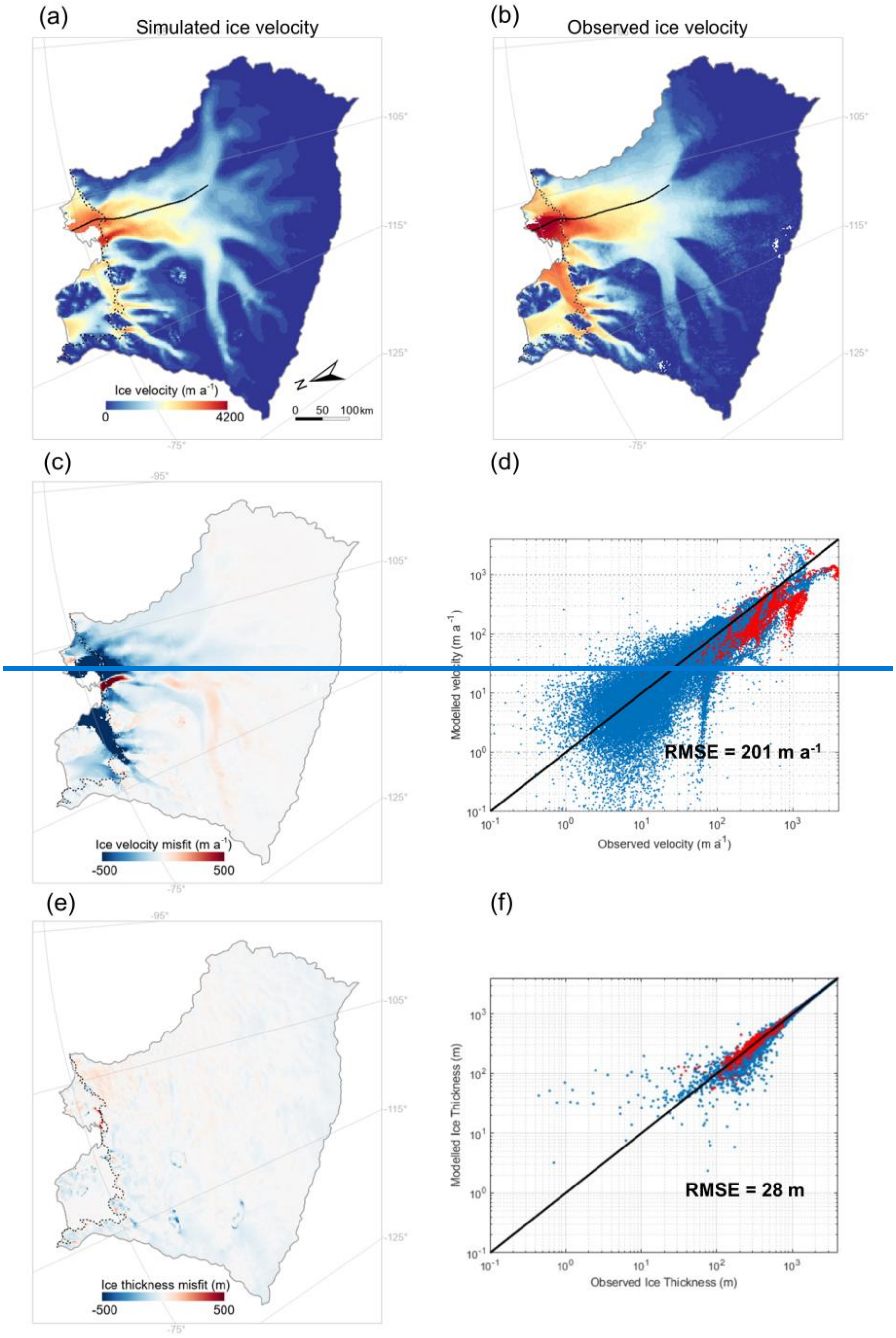

~~**Figure A1.** Simulated present-day state for the equilibrium initialization obtained with the 1995–2014 atmospheric climatology from MARv3.11 (Kittel et al., 2021). (a) Simulated ice velocity; (b) observed velocity (Rignot et al., 2017); (c) simulated minus observed ice velocity; (d) point-by-point scatter plots of simulated and observed ice sheet (blue) and ice shelf (red) velocities. The black curve is the flowline of Thwaites Glacier derived from the Antarctic surface flowline dataset developed by Liu et al. (2015). The black and gray dashed lines are observed (Gardner et al., 2018) and simulated grounding lines, respectively.~~

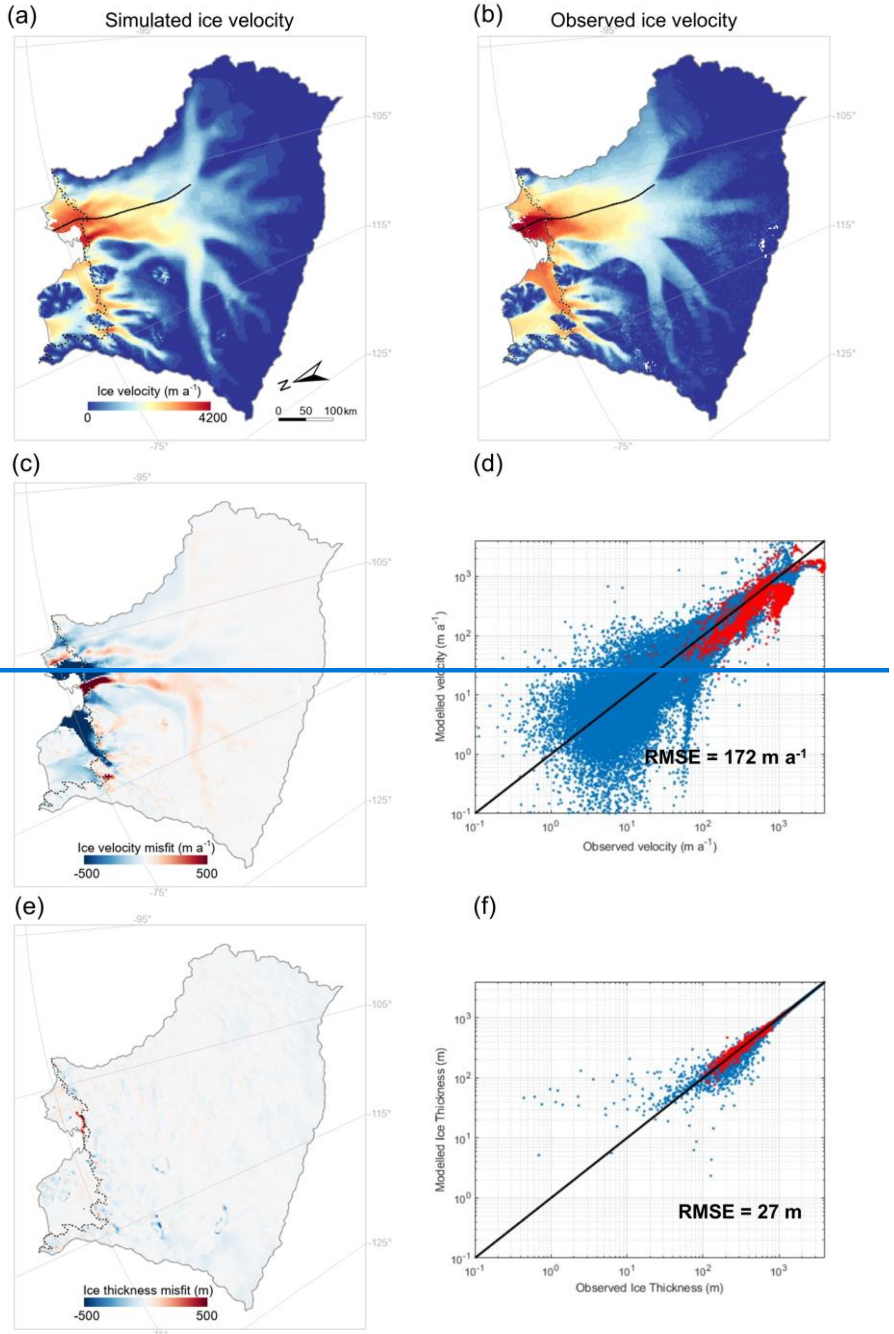

~~**Figure A2.** Simulated present-day state, same as Figure A1 but with mass balance correction using surface elevation change of the Amundsen Sea Embayment over the period 1992–2019 (Otosaka et al., 2023). (a) Simulated ice velocity; (b) observed velocity (Rignot et al., 2017); (c) simulated minus observed ice velocity; (d) point-by-point scatter plots of simulated and observed ice sheet (blue) and ice shelf (red) velocities. The black curve is the flowline of Thwaites Glacier derived from the Antarctic surface flowline dataset developed by Liu et al. (2015). The black and gray dashed lines are observed (Gardner et al., 2018) and simulated grounding lines, respectively.~~

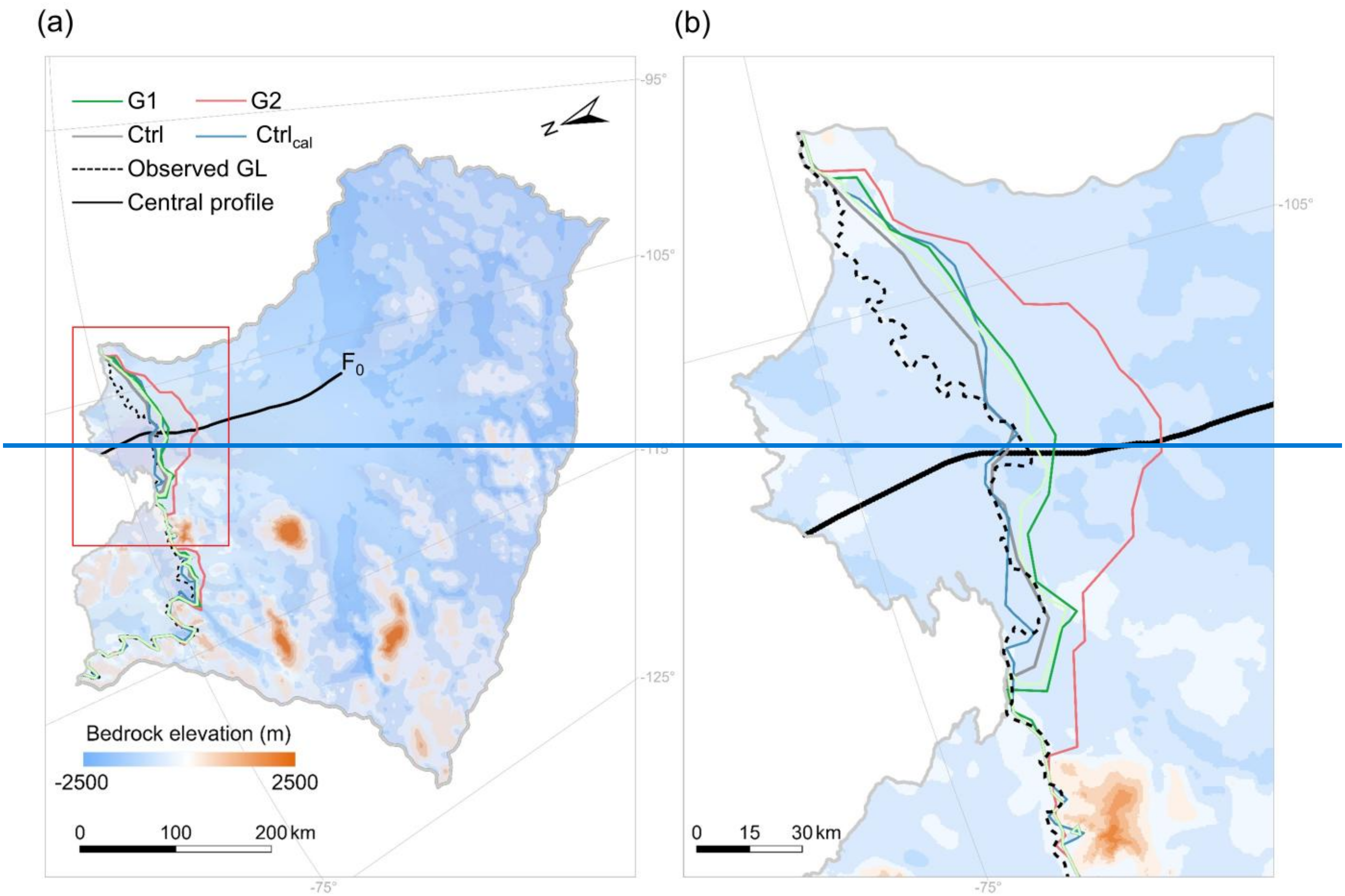

Figure A3. ~~Spatial pattern of the grounding-line position in the TG basin over the historical period 1990–2020 under different damage strengths. (a) Evolution of the grounding-line position within the TG basin and (b) an enlarged view of the red box in Figure (a). The light green and dark green lines represent the experiments with the least and the most grounding-line retreat in Group 1, respectively, and also correspond to the experiments with the lowest and highest damage strength in Group 1. The red line represents the experiment with the most grounding-line retreat in Group 2, and also corresponds to the experiment with the highest damage strength in Group 2 over the historical period 1990–2020. The black dashed line presents the observed grounding-line position (Gardner et al., 2018). The blue and grey lines present simulated grounding-line positions of the $\mathrm{Ctrl}_{\mathrm{cal}}$ and Ctrl experiments, respectively. The background figure in (a) is the observed bedrock elevation of the TG basin derived from BedMachine v2 data (Morlighem et al., 2020).~~

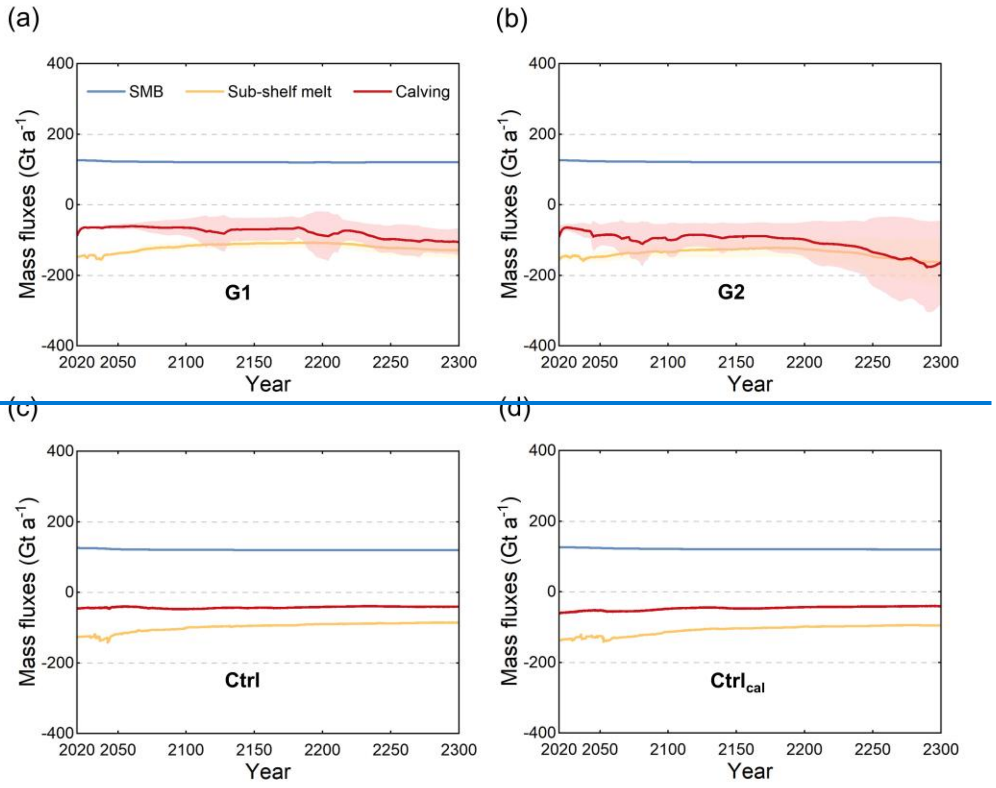

~~**Figure A4.** Evolution of the mass balance components including surface mass balance (SMB), the sub-shelf melt fluxes, and dynamic ice loss (i.e. the calving fluxes) under (a) Group 1, (b) Group 2, (c) Ctrl, and (d) Ctrl$_{cal}$ experiments over the projection period 2020–2300. Solid line represents mean, hatched area represents ensemble standard deviation.~~

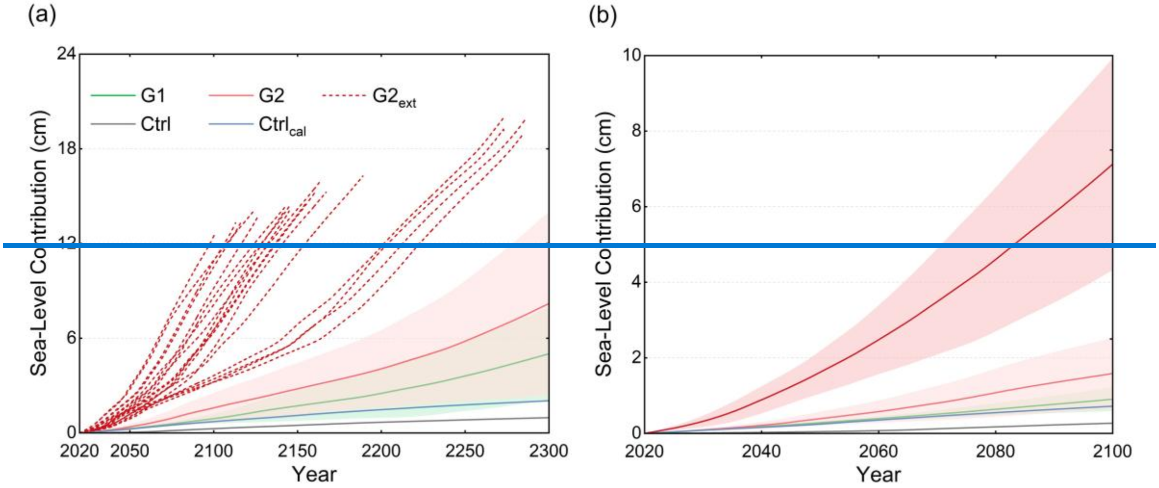

~~**Figure A5.** Evolution of the contribution to global mean sea-level rise of the TG basin over (a) the projection period 2020–2300, and (b) with a focus on the period 2020–2100 under constant present-day conditions. The dashed red lines in (a) represent experiments with higher~~

~~damage strengths that triggered a model collapse before 2300 and were grouped into Group 2 extreme experiments ($G2_{ext}$). Solid line represents mean, hatched area represents ensemble standard deviation.~~

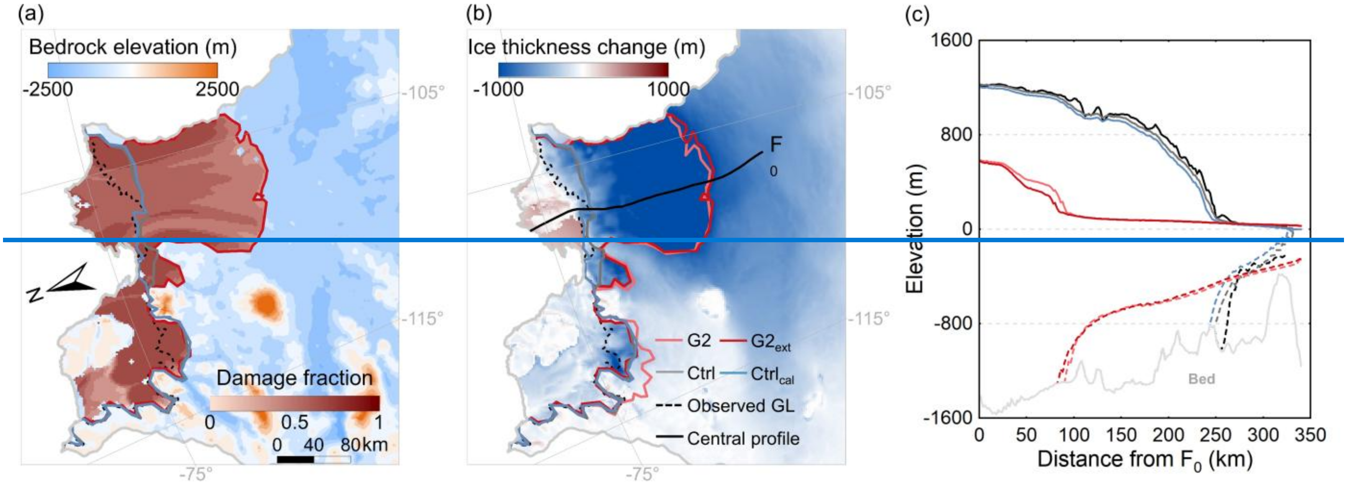

~~**Figure A6.** (a) Damage field, (b) ice thickness change, and (c) ice geometry along the central profile of the simulation with the highest damage strength in $G2_{ext}$ in the year 2100. The dark (light) red lines represent the spatial pattern of the simulated grounding line position and the ice geometry along the central profile of the simulation with the highest damage strength in $G2_{ext}$ (G2) in the year 2100 (2300). The black dashed line presents the observed grounding line position (Gardner et al., 2018). The blue and grey lines present simulated grounding line positions of the $Ctrl_{cal}$ and Ctrl experiments, respectively. The background figure in (a) is the observed bedrock elevation of the TG basin derived from BedMachine v2 data (Morlighem et al., 2020).~~

References

Albrecht, T. and Levermann, A.: Fracture field for large-scale ice dynamics, Journal of Glaciology, 58(207), 165-176, doi:10.3189/2012JoG11J191, 2012.

Albrecht, T. and Levermann, A.: Fracture-induced softening for large-scale ice dynamics, The Cryosphere, 8(2), 587-605, doi: 10.5194/tc-8-587-2014, 2014.

Bassis, J. N. and Ma, Y.: Evolution of basal crevasses links ice shelf stability to ocean forcing, Earth and Planetary Science Letters, 409, 203–211, doi:10.1016/j.epsl.2014.11.003, 2015.

Bassis, J. N. and Walker, C. C.: Upper and lower limits on the stability of calving glaciers from the yield strength envelope of ice, Proceedings of the Royal Society A: Mathematical, Physical and Engineering Sciences, 468(2140), 913-931, doi:10.1098/rspa.2011.0422: 2012.

Bassis, J. N., Berg, B., Crawford, A. J., and Benn, D. I.: Transition to marine ice cliff instability controlled by ice thickness gradients and velocity, Science, 372(6548), 1342-1344, doi:10.1126/science.abf627, 2021.

Benn, D. I. and Åström, J. A.: Calving glaciers and ice shelves, Advances in Physics, X3(1), 1513819, doi:10.1080/23746149.2018.1513819, 2018.

Bernales, J., Rogozhina, I., and Thomas, M.: Melting and freezing under Antarctic ice shelves from a combination of ice-sheet modelling and observations, Journal of Glaciology, 63(240), 731–744, doi:10.1017/jog.2017.42, 2017.

Bevan, S., Cornford, S., Gilbert, L., Otosaka, I., Martin, D., and Surawy-Stepney, T.: Amundsen Sea Embayment ice-sheet mass-loss predictions to 2050 calibrated using observations of velocity and elevation change, Journal of Glaciology, 69(278), 1729-1739, doi:10.1017/jog.2023.57, 2023.

Bindschadler, R., Vornberger, P., Fleming, A., Fox, A., Mullins, J., Binnie, D., Paulsen, S. J., Granneman, B., and Gorodetzky, D.: The Landsat image mosaic of Antarctica, Remote Sensing of Environment, 112(12), 4214-4226, doi:10.1016/j.rse.2008.07.006, 2008.

~~Bradley, A. T., Rydt, J. D., Bett, D. T., Dutrieux, P., and Holland, P. R.: The ice dynamic and melting response of Pine Island Ice Shelf to calving, Annals of Glaciology, 1–5, doi:10.1017/aog.2023.24, 2023.~~

Borstad, C., Khazendar, A., Larour, E., Morlighem, M., Rignot, E., Schodlok, M. P., and Seroussi, H.: A damage mechanics assessment of the Larsen B ice shelf prior to collapse: Toward a physically-based calving law, Geophysical Research Letters, 39(18), doi:10.1029/2012GL053317, 2012.

Cook, S., Rutt, I. C., Murray, T., Luckman, A., Zwinger, T., Selmes, N., Goldsack, A., and James, T. D.: Modelling environmental influences on calving at Helheim Glacier in eastern Greenland, The Cryosphere, 8(3), 827–841, doi:10.5194/tc-8-827-2014, 2014.

Cornford, S. L., Seroussi, H., Asay-Davis, X. S., Gudmundsson, G. H., Arthern, R., Borstad, C., Christmann, J., Dias dos Santos, T., Feldmann, J., Goldberg, D., Hoffman, M. J., Humbert, A., Kleiner, T., Leguy, G., Lipscomb, W. H., Merino, N., Durand, G., Morlighem, M., Pollard, D., Rückamp, M., Williams, C. R., and Yu, H.: Results of the third Marine Ice Sheet Model Intercomparison Project (MISMIP+), The Cryosphere, 14, 2283–2301, doi:10.5194/tc-14-2283-2020, 2020, 2020.

Coulon, V., Klose, A. K., Kittel, C., Edwards, T., Turner, F., Winkelmann, R., and Pattyn, F.: Disentangling the drivers of future Antarctic ice loss with a historically calibrated ice-sheet model, The Cryosphere, 18, 653–681, doi:10.5194/tc-18-653-2024, 2024.

DeConto. R. M. and Pollard, D.: Contribution of Antarctica to past and future sea-level rise, Nature, 531, 591-597, doi:10.1038/nature17145, 2016.

Duddu, R., Jiménez, S., and Bassis, J.: A non-local continuum poro-damage mechanics model for hydrofracturing of surface crevasses in grounded glaciers, Journal of Glaciology, 66(257), 415-429, doi:10.1017/jog.2020.16, 2020.

Gardner, A. S., Moholdt, G., Scambos, T., Fahnstock, M., Ligtenberg, S., van den Broeke, M., and Nilsson, J.: Grounding Line for Antarctic Discharge (GLAD) point files for flux estimates, available at: ftp://ftp.nsidc.org/pub/DATASETS/nsidc0732_landsat_antarctic_ice_velocities_v01/GardnerEtAl_2018_ SupData/GLAD_flux_gates/, last access: 9 July 2024, 2018.

Gerli, C., Rosier, S., and Gudmundsson, G. H~~., Krug, J., Durand, G., Favier,~~.: Activation ~~L.,~~ ~~and Gagliardini, O.: The stability~~ of existing surface crevasses has limited impact on grounding ~~lines on retrograde slopes, The Cryosphere, 6(6), 1497–1505, doi:10.5194/tc-6-1497-2012, 2012.~~

~~Gudmundsson, G. H., Paolo, F. S., Adusumilli, S., and Fricker, H. A.: Instantaneous~~line flux of Antarctic ice ~~sheet mass loss driven by thinning ice shelves,~~ streams, Geophysical Research Letters,~~ 46(23), 13903 – 13909~~ 50(6), e2022GL101687, doi:10.1029/~~2019GL085027, 2019~~2022GL101687, 2023.

Gudmundsson, G. H., Barnes, J. M., Goldberg, D. N., and Morlighem, M.: Limited Impact of Thwaites Ice Shelf on Future Ice Loss from Antarctica, Geophysical Research Letters, 50(11), e2023GL102880, doi:10.1029/2023GL102880, 2023.

Huth, A., Duddu, R., and Smith, B.: A generalized interpolation material point method for shallow ice shelves. 2: Anisotropic nonlocal damage mechanics and rift propagation, Journal of Advances in Modeling Earth Systems, 13(8), e2020MS002292, doi:10.1029/2020MS002292, 2021.

Huth, A., Duddu, R., Smith, B., and Sergienko, O.: Simulating the processes controlling ice-shelf rift paths using damage mechanics, Journal of Glaciology, 69(278), 1915 – 1928, doi: 10.1017/jog.2023.71, 2023.

Izeboud, M. and Lhermitte, S.: Damage detection on Antarctic ice shelves using the normalised radon transform, Remote Sensing of Environment, 284, 113359, doi:10.1016/j.rse.2022.113359, 2023.

Kachuck, S. B., Whitcomb, M., Bassis, J. N., Martin, D. F., and Price, S. F.: Simulating ice-shelf extent using damage mechanics, Journal of Glaciology, 68(271), 987-998, doi:10.1017/jog.2022.12, 2022.

Kazmierczak, E., Gregov, T., Coulon, V., and Pattyn, F.: A fast and unified subglacial hydrological model applied to Thwaites Glacier, Antarctica, EGUsphere~~,~~ [preprint], 2024, 1-36, doi:10.5194/egusphere-2024-466, 2024.

Khazendar, A., Rignot, E., and Larour, E.: Larsen B Ice Shelf rheology preceding its disintegration inferred by a control method, Geophysical Research Letters, 34, L19503, doi:10.1029/2007GL030980, 2007.

Kittel, C., Amory, C., Agosta, C., Jourdain, N. C., Hofer, S., Delhasse, A., Doutreloup, S., Huot, P.-V., Lang, C., Fichefet, T., and Fettweis, X.: Diverging future surface mass balance between the Antarctic ice shelves and grounded ice sheet, The Cryosphere, 15, 1215–1236, doi:10.5194/tc-15-1215-2021, 2021.

Laffin, M. K., Zender, C. S., van Wessem, M., and Marinsek, S.: The role of föhn winds in eastern Antarctic Peninsula rapid ice shelf collapse, The Cryosphere, 16(4), 1369–1381, doi:10.5194/tc-16-1369-2022, 2022.

Lhermitte, S., Sun, S., Shuman, C., Wouters, B., Pattyn, F., Wuite, J., Berthier, E., and Nagler, T.: Damage accelerates ice shelf instability and mass loss in Amundsen Sea Embayment, Proceedings of the National Academy of Sciences, 117(40), 24735-24741, doi:10.1073/pnas.1912890117, 2020.

Liu, Y., Moore, J. C., Cheng, X., Gladstone, R. M., Bassis, J. N., Liu, H., Wen, J., and Hui, F.: Ocean-driven thinning enhances iceberg calving and retreat of Antarctic ice shelves, Proceedings of the National Academy of Sciences, 112(11), 3263–3268, doi:10.1073/pnas.1415137112, 2015.

Miles, B. W. J., Stokes, C. R., Jenkins, A., Jordan, J. R., Jamieson, S. S. R., and Gudmundsson, G. H.: Intermittent structural weakening and acceleration of the Thwaites Glacier Tongue between 2000 and 2018, Journal of Glaciology, 66(257), 485–495, doi:10.1017/jog.2020.20, 2020.

Milillo, P., Rignot, E., Rizzoli, P., Scheuchl, B., Mouginot, J., Bueso-Bello, J., and Prats-Iraola, P.: Heterogeneous retreat and ice melt of Thwaites Glacier, West Antarctica. Science Advances, 5(1), eaau3433. doi:10.1126/sciadv.aau3433, 2019.

Moon, T., and Joughin, I.: Changes in ice front position on Greenland's outlet glaciers from 1992 to 2007, Journal of Geophysical Research: Earth Surface, 113(F2), doi:10.1029/2007JF000927, 2008.

Morlighem, M., Rignot, E., Binder, T., Blankenship, D., Drews, R., Eagles, G., Eisen, O., Ferraccioli, F., Forsberg, R., Fretwell, P., Goel, V., Greenbaum, J. S., Gudmundsson, H., Guo, J., Helm, V., Hofstede, C., Howat, I., Humbert, A., Jokat, W., Karlsson, N. B., Lee, W. S., Matsuoka, K., Millan, R., Mouginot, J., Paden, J., Pattyn, F., Roberts, J., Rosier, S., Ruppel, A., Seroussi, H., Smith, E. C., Steinhage, D., Sun, B., van den Broeke, M. R., van Ommen, T. D., van Wessem, M., and Young, D. A.: Deep glacial troughs and stabilizing ridges unveiled beneath the margins of the Antarctic ice sheet, Nature Geoscience, 13(2), 132–137, doi:10.1038/s41561-019-0510-8, 2020.

Morlighem, M., Goldberg, D., Barnes, J. M., Bassis, J. N., Benn, D. I., Crawford, A. J., Gudmundsson, G. H., and Seroussi, H.: The West Antarctic Ice Sheet may not be vulnerable to marine ice cliff instability during the 21st century, Science Advances, 10(34), eado7794, doi:10.1126/sciadv.ado7794, 2024.

Nick, F. M., van der Veen, C., Vieli, A., and Benn, D.: A physically based calving model applied to marine outlet glaciers and implications for the glacier dynamics, Journal of Glaciology, 56(199), 781–794. doi:10.3189/002214310794457344, 2011.

Nick, F. M., Vieli, A., Andersen, M. L., Joughin, I., Payne, A., Edwards, T. L., Pattyn, F., and van de Wal, R. S. W.: Future sea-level rise from Greenland’s main outlet glaciers in a warming climate, Nature, 497(7448), 235–238, doi:10.1038/nature12068, 2013.

Nye, J. F.: The distribution of stress and velocity in glaciers and ice-sheets, Proceedings of the Royal Society of London, Series A. Mathematical and Physical Sciences, 239(1216), 113–133, doi:10.1098/rspa.1957.0026, 1957.

~~Otosaka, I., Gilbert, L., and Shepherd, A.: Surface elevation change of the Amundsen Sea Embayment 1992-2019 [Data set], Zenodo, doi:10.5281/zenodo.8117577, 2023.~~

Pattyn, F. and Durand, G.: Why marine ice sheet model predictions may diverge in estimating future sea level rise, Geophysical research letters, 40(16), 4316-4320, doi:10.1002/grl.50824, 2013.

Pattyn, F.: Sea-level response to melting of Antarctic ice shelves on multi-centennial timescales with the fast Elementary Thermomechanical Ice Sheet model (f.ETISh v1.0), The Cryosphere, 11(4), 1851–1878, doi:10.5194/tc-11-1851-2017, 2017.

Pattyn, F.: The paradigm shift in Antarctic ice sheet modelling, Nature communications, 9(1), 2728, doi:10.1038/s41467-018-05003-z, 2018.

Pollard, D. and DeConto, R. M.: A simple inverse method for the distribution of basal sliding coefficients under ice sheets, applied to Antarctica, The Cryosphere, 6, 953–971, doi:10.5194/tc-6-953-2012, 2012.

Pollard, D., DeConto, R. M., and Alley, R. B.: Potential Antarctic Ice Sheet retreat driven by hydrofracturing and ice cliff failure, Earth and Planetary Science Letters, 412, 112–121, doi:10.1016/j.epsl.2014.12.035, 2015.

Ranganathan, M., Robel, A. A., Huth, A., and Duddu, R.: Glacier damage evolution over ice flow timescales, EGUsphere [preprint], https://doi.org/10.5194/egusphere-2024-1850, 2024.

Reese, R., Albrecht, T., Mengel, M, Asay-Davis, X., and Winkelmann, R.: Antarcticsub-shelf melt rates via PICO, The Cryosphere, 12(6), 1969-1985, doi:10.5194/tc-12-1969-2018, 2018.

Rignot, E., Mouginot, J., Morlighem, M., Seroussi, H., and Scheuchl, B.: Widespread, rapid grounding line retreat of Pine Island, Thwaites, Smith, and Kohler glaciers, West Antarctica, from 1992 to 2011, Geophysical Research Letters, 41(10), 3502 – 3509, doi:10.1002/2014GL060140, 2014.

Rignot, E., Mouginot, J. and Scheuchl, B.: MEaSUREs InSAR-Based Antarctica Ice Velocity Map, Version 2 [Date Accessed]. Boulder, Colorado USA. NASA National Snow and Ice Data Center Distributed Active Archive Center, doi:10.5067/D7GK8F5J8M8R, 2017.

Rignot, E., Mouginot, J., Scheuchl, B., van den Broeke, M., van Wessem, M. J., and Morlighem, M.: Four decades of Antarctic Ice Sheet mass balance from 1979–2017, Proceedings of the National Academy of Sciences, 116(4), 1095-1103, doi:10.1073/pnas.1812883116, 2019.

Robel, A. A.: Antarctica's ice cliff conundrum, Science Advances, **10**, eadr5921, doi:10.1126/sciadv.adr5921, 2024.

Schmidtko, S., Heywood, K. J., Thompson, A. F., and Aoki, S.: Multidecadal warming of Antarctic waters, Science, 346(6214), 1227-1231, doi:10.1126/science.1256117, 2014.

Schoof, C.: Ice sheet grounding line dynamics: Steady states, stability, and hysteresis, Journal of Geophysical Research: Earth Surface, 112(F3), doi:10.1029/2006JF000664, 2007.

Seroussi, H., Nowicki, S., Payne, A. J., Goelzer, H., Lipscomb, W. H., Abe-Ouchi, A., Agosta, C., Albrecht, T., Asay-Davis, X., Barthel, A., Calov, R., Cullather, R., Dumas, C., Galton-Fenzi, B. K., Gladstone, R., Golledge, N. R., Gregory, J. M., Greve, R., Hattermann, T., Hoffman, M. J., Humbert, A., Huybrechts, P., Jourdain, N. C., Kleiner, T., Larour, E., Leguy, G. R., Lowry, D. P., Little, C. M., Morlighem, M., Pattyn, F., Pelle, T., Price, S. F., Quiquet, A., Reese, R., Schlegel, N., Shepherd, A., Simon, E., Smith, R. S., Straneo, F., Sun, S., Trusel, L. D., Van Breedam, J., van de Wal, R. S. W., Winkelmann, R., Zhao, C., Zhang, T., and Zwinger, T.: ISMIP6 Antarctica: A multi-model ensemble of the Antarctic ice sheet evolution over the 21st century, The Cryosphere, 14(9), 3033–3070, doi:10.5194/tc-14-3033-2020, 2020.

Shepherd, A., Gilbert, L., Muir, A. S., Konrad, H., McMillan, M., Slater, T., Briggs, K. H., Sundal, A. V., Hogg, A. E., and Engdahl, M. E.: Trends in Antarctic Ice Sheet Elevation and Mass, Geophysical Research Letters, 46(14), 8174 – 8183, doi:10.1029/2019GL082182, 2019.

Sun, S., Cornford, S. L., Moore, J. C., Gladstone, R., and Zhao, L.: Ice shelf fracture parameterization in an ice sheet model, The Cryosphere, 11(6), 2543–2554, doi:10.5194/tc-11-2543-2017, 2017.

Sun, S., and Gudmundsson, G. H.: The speedup of Pine Island Ice Shelf between 2017 and 2020: revaluating the importance of ice damage. Journal of Glaciology, 1-9, doi:10.1017/jog.2023.76, 2023.

Surawy-Stepney, T., Hogg, A. E., Cornford, S. L., and Davison, B. J.: Episodic dynamic change linked to damage on the Thwaites Glacier Ice Tongue, Nature Geoscience, 16(1), 37–43, doi:10.1038/s41561-022-01097-9, ~~2023a~~2023.

~~Surawy-Stepney, T., Hogg, A. E., Cornford, S. L., and Hogg, D. C.: Mapping Antarctic crevasses and their evolution with deep learning applied to satellite radar imagery, The Cryosphere, 17, 4421–4445, doi:10.5194/tc-17-4421-2023, 2023b.~~

van de Wal, R. S. W., Nicholls, R. J., Behar, D., McInnes, K., Stammer, D., Lowe, J. A., Church, J. A., DeConto, R., Fettweis, X., Goelzer, H., Haasnoot, M., Haigh, I. D., Hinkel, J., Horton, B. P., James, T. S., Jenkins, A., LeCozannet, G., Levermann, A., Lipscomb, W. H., Marzeion, B., Pattyn, F., Payne, A. J., Pfeffer, W. T., Price, S. F., Seroussi, H., Sun, S., Veatch, W., and White, K.: A High-End Estimate of Sea Level Rise for Practitioners, Earth's Future, 10(11), e2022EF002751, doi:10.1029/2022EF002751, 2022.

van den Akker, T., Lipscomb, W. H., Leguy, G. R., Bernales, J., Berends, C., van de Berg, W. J., and van de Wal, R. S. W.: Present-day mass loss rates are a precursor for West Antarctic Ice Sheet collapse, ~~EGUsphere [preprint],~~The Cryosphere, 19, 283–301, doi:10.5194/~~egusphere-2024-851, 2024~~tc-19-283-2025, 2025.

Wesche, C.; Jansen, D.; Dierking, W.: Calving Fronts of Antarctica: Mapping and Classification, Remote Sensing, 5, 6305-6322, doi:10.3390/rs5126305, 2013.

Winkelmann, R., Martin, M. A., Haseloff, M., Albrecht, T., Bueler, E., Khroulev, C., and Levermann, A.: The Potsdam Parallel Ice Sheet Model (PISM-PIK) – Part 1: Model description, The Cryosphere, 5, 715–726, doi:10.5194/tc-5-715-2011, 2011.

Zwally, H. J., Li, J., Robbins, J. W., Saba, J. L., Yi, D., and Brenner, A. C.: Mass gains of the Antarctic ice sheet exceed losses, Journal of Glaciology, 61(230), 1019–1036, doi:10.3189/2015JoG15J071, 2015.